significant, dose-dependent, concentration-dependent, and visually evident changes in cardiac contractility as indicated by increases in FS (Fig. 4A and movie S1) (*19*).

Omecamtiv mecarbil improved left ventricular systolic function in a conscious canine model with chronically implanted sensors to assess LV dimensions, atrial and arterial pressures, and stroke volume (*20*). The direct effect on cardiac contractility was evident from the increase in myocardial wall thickening (WT) and FS (Fig. 4B) in the absence of a change in loading conditions, such as mean arterial pressure, LV end diastolic pressure, and total vascular resistance (–2.2 ± 1.3%, –7.3 ± 5.8%, and –2.4 ± 2.3%, means ± SEM, $P > 0.05$). In dogs with heart failure induced by chronic fast pacing of heart rate in concert with a localized myocardial infarction (*21*), omecamtiv mecarbil produced substantially greater and statistically significant ($P < 0.01$) increases in stroke volume (60.8 ± 12.5%) and cardiac output (29.1 ± 6.1%) than it did in normal dogs (10.2 ± 3.6% and 0.8 ± 2.0%, respectively). The increase in cardiac output was especially notable given the coincident lowering of heart rate (–16.7 ± 4.0%, $P = 0.014$) observed in the dogs with heart failure (Fig. 4B; P calculated using Student's t test).

Underlying the effects on systolic function was an increase in systolic ejection time (SET) in the absence of changes in the rate of LV pressure development (dP/dt) (Fig. 4B). In contrast, existing drugs, such as the β-adrenergic agonist dobutamine, increase cardiac contractility by increasing dP/dt and shortening SET (*22*). We investigated this finding further by comparing omecamtiv mecarbil with dobutamine, using time-dependent LV end systolic elastance, a load-independent measure of cardiac contractility derived from the pressure-volume loop (*23*). The plots of time-dependent elastance (Fig. 4C) are illustrative of the different effects that the two drug mechanisms have on the dynamics of cardiac contractility.

Overall energy balance in the contracting heart is set by a combination of loading conditions, heart rate, membrane ion fluxes, calcium cycling, and crossbridge cycling. Although omecamtiv mecarbil might increase ATP turnover at the level of the sarcomere, on balance, myocardial energetics appear unchanged following omecamtiv mecarbil administration, as it does not increase overall myocardial oxygen consumption (*8*) at doses producing substantial improvements in cardiac function. However, excessive crossbridge activation at excessive doses of omecamtiv mecarbil could lead to an increase in the duration of systole to an extent where coronary blood flow during diastole is reduced, and signs and symptoms of cardiac ischemia may emerge.

As a selective, allosteric activator of cardiac myosin, omecamtiv mecarbil is a rare example of a drug mechanism whose action depends on activation rather than inhibition of an enzyme, an approach that may have broader application for therapeutic intervention (*24*–*26*). It represents a therapeutic approach to directly improve cardiac function that potentially avoids the deleterious effects limiting current indirect inotropic mechanisms (*27*). Further studies in patients with heart failure will eventually define the clinical benefit and risk profile of cardiac myosin activation in a condition that is still marked by substantial rates of mortality and morbidity.

References and Notes

1. D. Lloyd-Jones *et al.*, *Circulation* **121**, 948 (2010).
2. L. R. Loehr, W. D. Rosamond, P. P. Chang, A. R. Folsom, L. E. Chambless, *Am. J. Cardiol.* **101**, 1016 (2008).
3. K. F. Adams Jr. *et al.*, *Am. Heart J.* **149**, 209 (2005).
4. J. J. V. McMurray, *N. Engl. J. Med.* **362**, 228 (2010).
5. D. A. Kass, R. J. Solaro, *Circulation* **113**, 305 (2006).
6. T. Pollard, W. Earnshaw, *Cell Biology* (Saunders/Elsevier, Philadelphia, ed. 2, 2008) pp. 705–725.
7. B. P. Morgan *et al.*, *ACS Med Chem Lett.* **1**, 472 (2010).
8. Y. T. Shen *et al.*, *Circ Heart Fail.* **3**, 522 (2010).
9. Materials and methods are available as supporting material on *Science* Online.
10. R. W. Lymn, E. W. Taylor, *Biochemistry* **10**, 4617 (1971).
11. H. L. Sweeney, A. Houdusse, *Annu. Rev. Biophys.* **39**, 539 (2010).
12. K. C. Holmes, I. Angert, F. J. Kull, W. Jahn, R. R. Schröder, *Nature* **425**, 423 (2003).
13. M. Brune, J. L. Hunter, J. E. Corrie, M. R. Webb, *Biochemistry* **33**, 8262 (1994).
14. E. M. De La Cruz, E. M. Ostap, *Methods Enzymol.* **455**, 157 (2009).
15. T. Suzuki *et al.*, *Circ. Heart Fail.* **2**, 334 (2009).
16. Single-letter abbreviations for the amino acid residues are as follows: A, Ala; C, Cys; D, Asp; E, Glu; F, Phe; G, Gly; H, His; I, Ile; K, Lys; L, Leu; M, Met; N, Asn; P, Pro; Q, Gln; R, Arg; S, Ser; T, Thr; V, Val; W, Trp; and Y, Tyr.
17. I. Rayment *et al.*, *Science* **261**, 50 (1993).
18. L. Cleemann, M. Morad, *J. Physiol.* **432**, 283 (1991).
19. In the online materials, a side-by-side movie shows several heartbeats of a short-axis echocardiogram in an anesthetized beagle before (on the left) and after (on the right) a 1-hour infusion of omecamtiv mecarbil at 1 mg/kg of body weight per hour. In this view, the left ventricular cavity is in the middle of a ring of contracting myocardium.
20. K. Komamura *et al.*, *J. Clin. Invest.* **89**, 1825 (1992).
21. Y. T. Shen, J. J. Lynch, R. P. Shannon, R. T. Wiedmann, *Am. J. Physiol.* **277**, H388 (1999).
22. P. N. Banfor *et al.*, *Am. J. Physiol. Heart Circ. Physiol.* **294**, H238 (2008).
23. H. Suga, K. Sagawa, *Circ. Res.* **35**, 117 (1974).
24. J. Grimsby *et al.*, *Science* **301**, 370 (2003).
25. J. P. Stasch *et al.*, *Br. J. Pharmacol.* **136**, 773 (2002).
26. J. A. Zorn, J. A. Wells, *Nat. Chem. Biol.* **6**, 179 (2010).
27. J. W. Petersen, G. M. Felker, *Crit. Care Med.* **36** (suppl.), S106 (2008).

28. We thank J. Chabala, C. Homcy, T. A. Pollard, J. H. Sabry, R. J. Solaro, J. A. Spudich, J. R. Teerlink, and R. D. Vale for their advice over the course of this work; A. Franklin and S. Hollenbach for their contributions to the conduct of some of these studies; and M. Rowley and J. Goldstein for assistance in preparing the manuscript. Y.-T.S., D.A.K., and S.F.V. are members of the Scientific Advisory Board and received research support, compensation, and stock options (D.A.K. and S.F.V.) from Cytokinetics. Cytokinetics holds a patent on omecamtiv mecarbil (U.S. Patent no. 7,507,735); Amgen is a licensee of this patent. Support provided by Small Business Innovation Research grant, NIH (1-R43-HL-66647-1) and Cytokinetics, Inc.

Supporting Online Material

www.sciencemag.org/cgi/content/full/331/6023/1439/DC1
Materials and Methods
Figs. S1 to S9
Tables S1 to S3
References
Movie S1

8 November 2010; accepted 18 January 2011
10.1126/science.1200113

Reversal of Interlaminar Signal Between Sensory and Memory Processing in Monkey Temporal Cortex

Daigo Takeuchi, Toshiyuki Hirabayashi, Keita Tamura, Yasushi Miyashita*

The primate temporal cortex implements visual long-term memory. However, how its interlaminar circuitry executes cognitive computations is poorly understood. Using linear-array multicontact electrodes, we simultaneously recorded unit activities across cortical layers in the perirhinal cortex of macaques performing a pair-association memory task. Cortical layers were estimated on the basis of current source density profiles with histological verifications, and the interlaminar signal flow was determined with cross-correlation analysis between spike trains. During the cue period, canonical "feed-forward" signals flowed from granular to supragranular layers and from supragranular to infragranular layers. During the delay period, however, the signal flow reversed to the "feed-back" direction: from infragranular to supragranular layers. This reversal of signal flow highlights how the temporal cortex differentially recruits its laminar circuits for sensory and mnemonic processing.

The primate inferotemporal cortex locates at the final stage of the ventral visual pathway and serves as a storehouse for visual long-term memory (*1*–*4*). Previous studies have demonstrated neuronal activity related to presented visual objects and retrieved images at the single-neuron level (*4*–*6*), but the underlying network dynamics (*7*–*12*) remain to be understood. Evidence from the primary sensory cortices suggests that local circuits extending across cortical layers are crucially involved in sensory processing (*13*–*15*).

Department of Physiology, University of Tokyo School of Medicine, 7-3-1 Hongo, Bunkyo-ku, Tokyo 113-0033, Japan.

*To whom correspondence should be addressed. E-mail: yasushi_miyashita@m.u-tokyo.ac.jp

This raises questions about how the interlaminar circuitry in the inferotemporal cortex is differentially recruited to process presented objects and to retrieve visual long-term memory.

We used two strategies to investigate interlaminar signal flow in awake behaving monkeys. First, we used current source density (CSD) analysis as a tool for layer estimation in each electrode penetration; CSD reflects the gross transmembrane currents in the local neuronal ensemble and is used to estimate the cortical layers that receive afferent inputs (*16*, *17*). Second, we used cross-correlation analysis of spike trains (*18*–*21*) to infer the functional interactions across cortical layers; asymmetry or peak lag of the cross-correlogram (CCG) reflects the direction of functional connectivity between neurons (*22*, *23*).

Two monkeys were trained to perform a pair-association task, in which they had to retrieve the learned paired associate in response to the presented cue stimulus (Fig. 1A) (*3*–*5*). We recorded single- and multi-unit activities and local field potentials (LFPs) by inserting linear-array multicontact electrodes (16 or 24 contacts with spacing of 150 or 100 μm, respectively) vertically (table S1) (*24*) into area 36 (A36) (Fig. 1B). CSD was then calculated from depth profiles of stimulus-evoked LFPs in order to physiologically estimate the position of the granular layer (*24*). A representative CSD profile exhibited the earliest current sink (Fig. 1, D and E, asterisks) at the contact corresponding to the histologically verified granular layer (Fig. 1C, red). This earliest current sink was followed by sinks at more superficial contacts and by sources at deeper contacts (Fig. 1D). Similar CSD profiles were consistently observed for all penetrations (fig. S1). Postmortem histological analyses (*24*) confirmed that the earliest current sink evoked by cue stimuli consistently corresponded to the granular layer [table S1, the distance between the contact with the earliest current sink ("earliest-sink contact"), and the center of the granular layer was 79 μm (median), $n = 6$ penetrations]. The histological verifications, together with consistent CSD profiles across penetrations, demonstrated that the CSD profiles can be reliably used to estimate the granular layer (G), the supragranular layer (SG), and the infragranular layer (IG) (*24*). In this representative penetration, single unit activities were simultaneously recorded in SG and IG (Fig. 1, F and G), both showing stimulus-selective responses during the cue period (Fig. 1H). The CCG (*18*–*23*) for this unit pair exhibited a significant displaced peak (4 ms lag) on the right side (Fig. 1I), suggesting a functional connectivity from the SG unit to the IG unit, which is consistent with the "feed-forward" signal flow in the primary sensory cortices (*13*–*15*).

We made 20 penetrations in three hemispheres of two monkeys and conducted cross-correlation analyses for three populations of unit pairs: G-SG pairs (cue period, $n = 52$ pairs; delay-period, $n = 49$ pairs), G-IG pairs ($n = 128$ pairs; $n = 121$ pairs), and SG-IG pairs ($n = 252$ pairs; $n = 211$ pairs) [both single units and multi-units were included; for details, see supporting online material (SOM) text and table S2]. A CCG was calculated only when both constituent units responded to at least one common stimulus during either the cue or delay period. CCG peak was detected within 10 ms lag (*19*–*22*) so as to evaluate its significance ($Z > 2.82$, $P < 0.05$) (*24*). We then compared the proportions of unit pairs with significant CCG peaks among the G-SG, G-IG, and SG-IG pairs (fig. S2). The proportion of unit pairs with a significant CCG peak was greater for G-SG pairs than for G-IG pairs during both the cue period (33% versus 11%; χ^2 test with post-hoc pair-wise comparisons followed by Bonferroni's correction, $P < 0.005$) and delay period (27% versus 12%; $P < 0.05$). The proportion of unit pairs with a significant CCG peak was greater for G-SG pairs than for SG-IG pairs during the cue period (33% versus 16%;

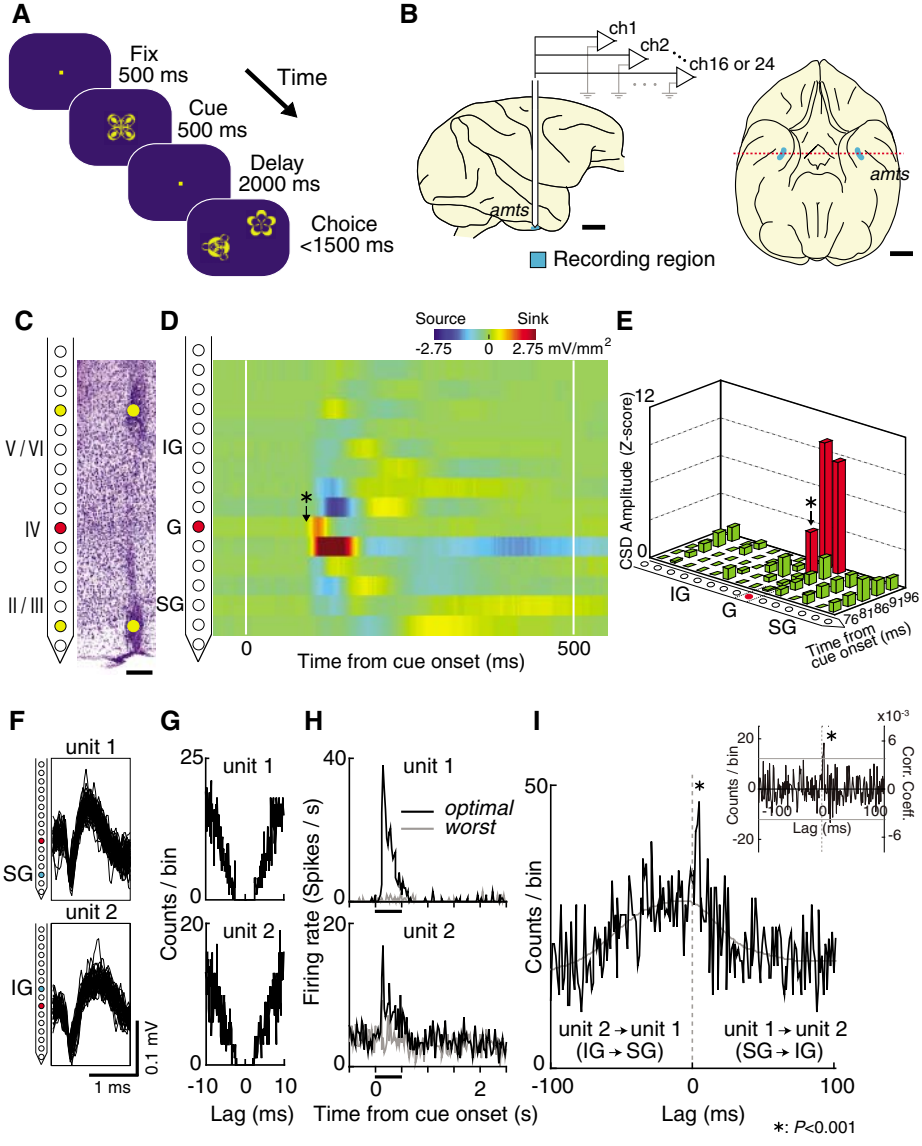

Fig. 1. (**A**) Sequence of pair-association task. Monkeys had to retrieve the learned paired associate in response to the presented cue stimulus. (**B**) Lateral (left) and ventral (right) views of monkey brain. Unit activities and LFPs were recorded across cortical layers in area 36 (blue) by using a linear-array multicontact electrode. Scale bar, 10 mm; amts, anterior middle temporal sulcus. (**C** to **I**) A representative data set. (C) Electrolytic lesion marks made at two contacts of the electrode (yellow contacts) were identified in a Nissl-stained histological section. Scale bar, 200 μm. [(D) and (E)] Stimulus-evoked CSDs. The earliest significant current sink appeared at 91 ms after cue onset (asterisks), (red contact). The red contact corresponded to the granular layer in histological section (C). Red and green bars in (E) indicate significant and nonsignificant current sink, respectively. G, SG, and IG represent granular, supragranular, and infragranular layers, respectively. (F) Waveforms, (G) auto-correlograms, and (H) poststimulus time histograms of two single units simultaneously recorded in SG and IG [(F), blue contacts]. (I) Raw CCG between spike trains of the SG and IG units in the cue period (black line). Gray line, IFR-predictor (*24*). Bin width, 1 ms. (Inset) IFR-predictor–subtracted CCG. The CCG exhibited a significant peak on the right side (lag time, 4 ms). Horizontal gray line indicates the confidence limit.

$P < 0.05$), and the same tendency was observed during the delay period (27% versus 19%; $P = 0.24$).

We next examined the direction of functional connectivity between units in different layers during each task period. For G-SG pairs, the distribution of asymmetry index (AI) (*22*–*24*) of individual CCGs during the cue period was shifted to the feed-forward direction: from G to SG (Fig. 2B, blue) [Wilcoxon signed-rank test; cue period (Fig. 2B, blue), $P < 0.01$, $n = 17$ pairs]. This directional bias was not significant during the delay period (Fig. 2B, red) ($P > 0.4$, $n = 14$ pairs). Similar results were obtained using the center of mass (CoM) of the CCG peak (Fig. 2C) [cue period (Fig. 2C, blue), $P < 0.04$; delay period (Fig. 2C, red), $P > 0.5$]. During the fix period, only four pairs exhibited a significant CCG peak, and thus the directional bias was not statistically evaluated. These results were further substantiated by the population-averaged CCGs (Fig. 2A and fig. S4A): The CCG showed a prominent peak [$P < 0.001$, (*24*)] on the right side during the cue period (G to SG) (Fig. 2A, blue). In G-IG pairs, no bias was observed in their signal flow directions during any of the task periods (fig. S3).

We repeated the same analyses for SG-IG pairs (Fig. 2, E to G). The distribution of AIs during the cue period was significantly shifted toward the direction from SG to IG (Fig. 2F, blue) ($P < 0.01$, $n = 41$ pairs). However, the distribution during the delay period exhibited a bias in the opposite direction, IG toward SG (Fig. 2F, red) ($P < 0.01$, $n = 41$ pairs). No significant directional bias was observed during the fix period ($P > 0.2$, $n = 12$ pairs). Similar results were obtained using the CoM [cue period (Fig. 2G, blue), $P < 0.03$; delay-period (Fig. 2G, red), $P < 0.02$; fix-period, $P > 0.8$] (*24*). Population-averaged CCGs again confirmed these results (Fig. 2E and fig. S4B): During the cue period, a significant peak was observed on the right side ($P < 0.001$; SG to IG, Fig. 2E, blue), whereas a significant peak appeared on the left side during the delay period ($P < 0.001$; IG to SG, Fig. 2E, red). Consistent results were obtained using only single unit data (SOM text and fig. S5).

These results demonstrated the signal flow from G to SG and from SG to IG during the cue period, as in the canonical feed-forward processing (Fig. 2, D and H, left) (*13*–*15*). During the delay period, however, the direction of signal flow reversed, suggesting recruitment of a "feedback" pathway (Fig. 2H, right).

We then examined the temporal dynamics of the functional connectivity for individual SG-IG pairs. Figure 3A shows the time course of the correlation strength (CS) and asymmetry index (AI) for each pair ($n = 70$ pairs) that exhibited a significant peak during either the cue or delay period (*24*). Although the connectivity of individual pairs exhibited a variety of dynamics, as a whole the direction of connectivity gradually changed: SG to IG (Fig. 3A, blue) during the cue period and IG to SG (Fig. 3A, orange) during the delay period (Fig. 3B) (for the temporal dynamics of firing rates, see SOM text and figs. S6 and S7). To investigate these observations quantitatively, we divided SG-IG pairs according to the sign of the AI in the cue and delay periods. Nearly half of the pairs (47%, 33 of 70) exhibited directional changes in the connectivity between the cue and delay periods ("flipped pairs") (Fig. 3C), suggesting that the signal flow direction can be modulated in individual pairs. Of these, a significantly greater proportion (73%, 24 of 33 pairs; χ^2 test, $P < 0.01$) exhibited connectivity from SG to IG during the cue period and reversed their direction during the delay period. Furthermore, unit pairs that did not change the sign of AI between the cue and delay periods ("non-flipped pairs"; 53%, 37 of 70 pairs) also contributed to the overall changes in the signal flow (Fig. 3D): For unit pairs with connectivity direction from SG to IG (Fig. 3D, blue), AIs in the delay period were closer to zero than those in the cue period (Wilcoxon signed-rank test, $P < 0.05$, $n = 17$ pairs), and for unit pairs with connectivity direction from IG to SG (Fig. 3D, orange), AIs in the delay period were more negative than those in the cue period ($P < 0.01$, $n = 20$ pairs). Together, the reversal of connectivity direction between the cue and delay periods (Fig. 2) was the result of both the directional changes of the flipped pairs and consistent small directional shifts of the non-flipped pairs.

Lastly, we examined the spatial patterns of functional connectivity by calculating the laminar

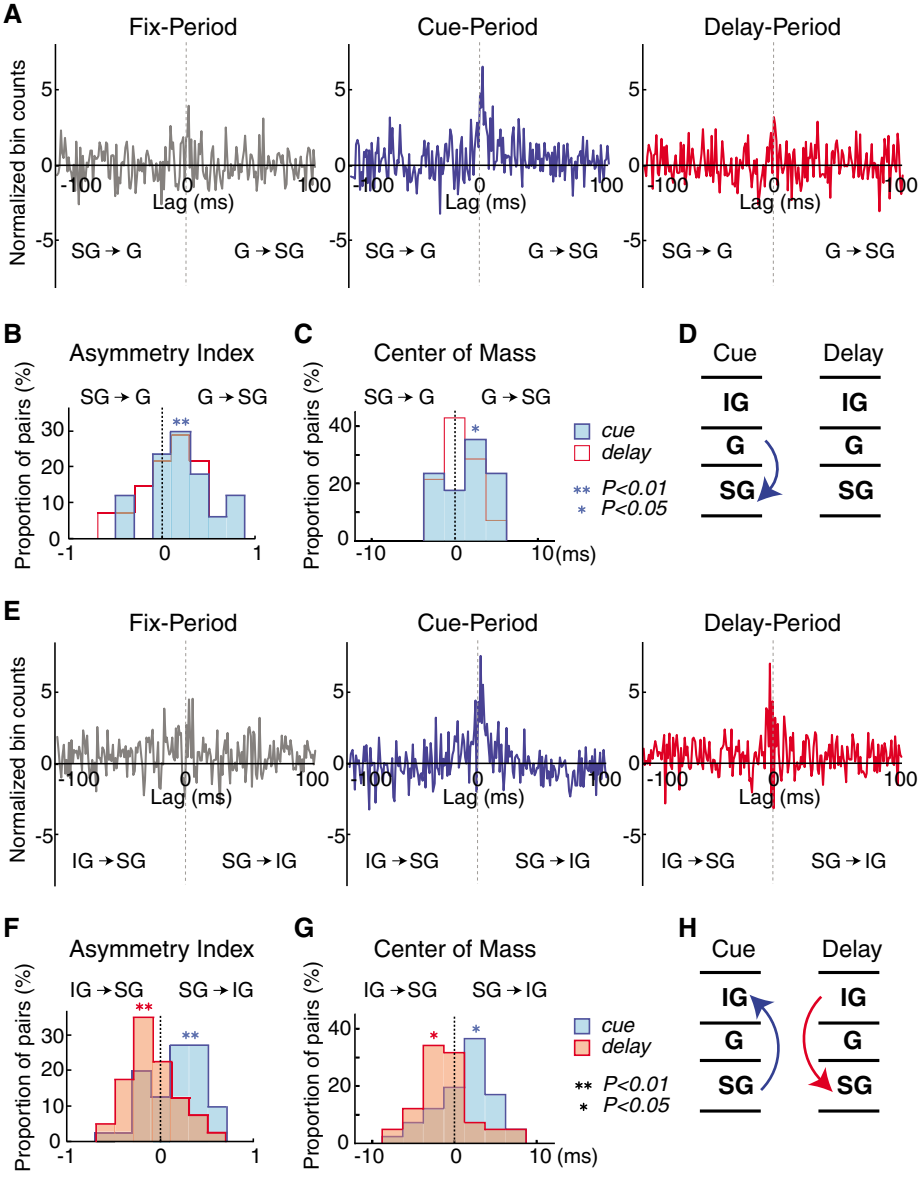

Fig. 2. Population results of the functional connectivity. (**A** to **C**) Cross-correlation between spike trains of G-SG pairs. (A) Population-averaged CCGs in the (gray, left) fix, (blue, middle) cue, and (red, right) delay periods, respectively. (B) Asymmetry index and (C) center of mass of individual CCGs. Asterisk indicates significant bias to either side of the histogram. Filled histogram indicates a task period for which significant bias in the directionality was observed. (**D**) Schematic diagram of interlaminar signal flow between G and SG. (**E** to **H**) Same as in (A) to (D), but for SG-IG pairs.

positions of units by parametrically using the distances from the estimated granular layer (Fig. 4 and fig. S8) (*25*, *26*). Compared with the connectivity during the fix period, two prominent connectivity patterns appeared during the cue period, corresponding to the feed-forward pathways from G to SG and from SG to IG (Fig. 4, A and B, middle). During the delay period, the feed-forward connectivity was attenuated, and the feed-back connectivity from IG to SG emerged (Fig. 4, A and B, right). In addition, outward signal flow (from superficial to deep parts) within IG was found during the delay period (Fig. 4, A and B, right). Putative target units of this outward flow were located at significantly deeper positions than those of the putative source

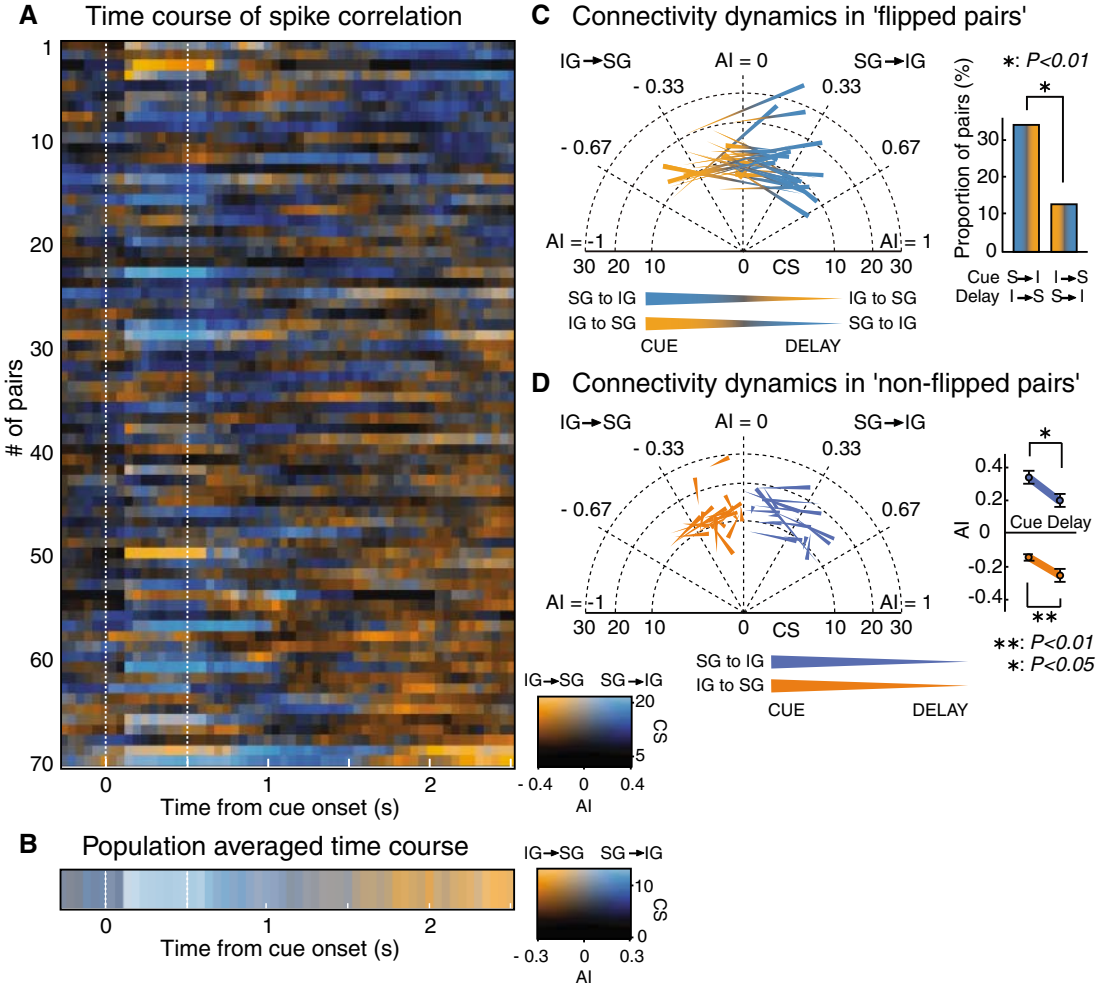

Fig. 3. Connectivity dynamics of individual SG-IG pairs. (**A**) Time course of spike correlation for individual unit pairs. AI and CS of CCGs were color-coded as shown in the inset. Unit pairs were sorted according to AI value during the latter half of the delay period. (**B**) Population average of all the unit pairs. (**C** and **D**) Polar plot of CS and AI dynamics for the (C) flipped- and (D) non-flipped pairs. Radius, CS. Angle from the vertical axis, AI. Positions of base and tip of an arrow correspond to AI/CS values during cue and delay periods, respectively. [(C), right] Proportion of each type of flipped pairs. S and I represent SG and IG, respectively. [(D), right] AI of non-flipped pairs during the cue and delay periods. Blue, SG→IG pairs; orange, IG→SG pairs.

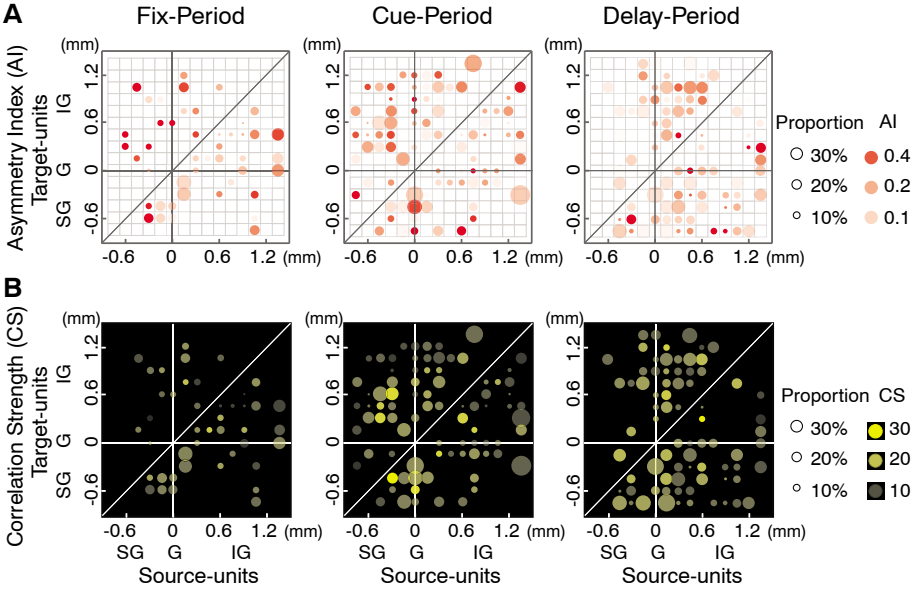

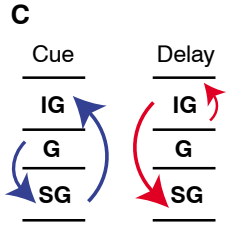

Fig. 4. Interlaminar connectivity matrices. (**A**) AI matrix for each task period. Abscissa and ordinate represent recorded positions of the putative source and target units relative to the earliest-sink contact, respectively. Size of a circle in each matrix indicates the proportion of unit pairs with significant CCG peak to the total number of unit pairs for which CCGs were calculated at the corresponding site. Saturation of color of each circle indicates the average of AI across unit pairs. (**B**) CS matrix, as in (A). All laminar positions plotted in the AI and CS matrices were recorded in at least three penetrations. (**C**) Summary diagrams showing all the laminar signal flows identified in the present study.

units (fig. S9) [paired t test, $P < 0.02$, $n = 19$ pairs; median distances from the granular layer were 0.45 mm (source units) and 1.05 mm (target units)].

The present study demonstrated that canonical feed-forward signal flow across cortical layers during sensory coding reverse to the feed-back direction during memory retrieval phase, which suggests flexible recruitment of interlaminar connectivity depending on the cognitive demands in the monkey association cortices (Fig. 4C). We used CSD analysis to estimate cortical layers (Fig. 1, C to E, and fig. S1), and the observed stimulus-evoked CSD profiles were quite similar to those in the primary sensory cortices (*17*, *27*). For some penetrations, we observed that the current sink positioned superficially next to the earliest-sink contact exhibited larger peak amplitudes and much longer durations than that of the earliest current sink. This observation might reflect the cytoarchitectural nature of A36 as a dysgranular cortex (*28*) as well as the direct inputs to the deepest part of the superficial layer, which is consistent with anatomical observations (*29*).

A recent study in the rat primary auditory cortex demonstrated that the direction of interlaminar signal flow depends on the cortical "state": Sensory-evoked responses were initiated in the thalamorecipient layers and then propagated to the superficial and deep layers, whereas in spontaneously active "up-states," neuronal activity was initiated in the deep layers and then propagated to the superficial layers (*27*). These state-dependent changes in the interlaminar signal flows in rats are consistent with our results obtained in monkeys performing a memory task. Together, these findings highlight the flexibility of cortical laminar circuits. Further experiments will be needed to determine whether such flexible interlaminar connectivity is also implemented and used in other cortical areas for other cognitive demands.

References and Notes

1. L. R. Squire, J. T. Wixted, R. E. Clark, *Nat. Rev. Neurosci.* **8**, 872 (2007).
2. W. A. Suzuki, *Neuron* **61**, 657 (2009).
3. E. A. Murray, T. J. Bussey, L. M. Saksida, *Annu. Rev. Neurosci.* **30**, 99 (2007).
4. Y. Miyashita, *Science* **306**, 435 (2004).
5. Y. Naya, M. Yoshida, Y. Miyashita, *J. Neurosci.* **23**, 2861 (2003).
6. N. K. Logothetis, D. L. Sheinberg, *Annu. Rev. Neurosci.* **19**, 577 (1996).
7. G. Buzsáki, *Neuron* **68**, 362 (2010).
8. S. H. Wang, R. G. Morris, *Annu. Rev. Psychol.* **61**, 49, C1 (2010).
9. M. P. Witter, E. I. Moser, *Trends Neurosci.* **29**, 671 (2006).
10. A. Bollimunta, Y. Chen, C. E. Schroeder, M. Ding, *J. Neurosci.* **28**, 9976 (2008).
11. A. K. Engel, P. Fries, *Curr. Opin. Neurobiol.* **20**, 156 (2010).
12. I. E. Ohiorhenuan *et al.*, *Nature* **466**, 617 (2010).
13. R. J. Douglas, K. A. Martin, *Annu. Rev. Neurosci.* **27**, 419 (2004).
14. J. J. Nassi, E. M. Callaway, *Nat. Rev. Neurosci.* **10**, 360 (2009).
15. R. C. Reid, J. M. Alonso, *Curr. Opin. Neurobiol.* **6**, 475 (1996).
16. J. Csicsvari, B. Jamieson, K. D. Wise, G. Buzsáki, *Neuron* **37**, 311 (2003).
17. C. E. Schroeder, P. Lakatos, *Trends Neurosci.* **32**, 9 (2009).
18. A. K. Engel, W. Singer, *Trends Cogn. Sci.* **5**, 16 (2001).
19. T. Hirabayashi, Y. Miyashita, *J. Neurosci.* **25**, 10299 (2005).
20. M. Tomita, J. J. Eggermont, *J. Neurophysiol.* **93**, 378 (2005).
21. C. A. Atencio, C. E. Schreiner, *PLoS ONE* **5**, e9521 (2010).
22. T. Hirabayashi, D. Takeuchi, K. Tamura, Y. Miyashita, *J. Neurosci.* **30**, 10407 (2010).
23. J. M. Alonso, L. M. Martinez, *Nat. Neurosci.* **1**, 395 (1998).
24. Materials and methods are available as supporting material on *Science* Online.
25. S. Lefort, C. Tomm, J. C. Floyd Sarria, C. C. H. Petersen, *Neuron* **61**, 301 (2009).
26. N. Weiler, L. Wood, J. I. Yu, S. A. Solla, G. M. G. Shepherd, *Nat. Neurosci.* **11**, 360 (2008).
27. S. Sakata, K. D. Harris, *Neuron* **64**, 404 (2009).
28. W. A. Suzuki, D. G. Amaral, *J. Comp. Neurol.* **463**, 67 (2003).
29. K. S. Saleem, K. Tanaka, *J. Neurosci.* **16**, 4757 (1996).

30. This work was supported by a Grant-in-Aid for Specially Promoted Research from the Ministry of Education, Culture, Sports, Science and Technology (MEXT) to Y.M. (19002010) and Grant-in-Aid for Young Scientists from MEXT to T.H. (18700378); a grant from Takeda Science Foundation to Y.M.; and Japan Society for the Promotion of Science (JSPS) Research Fellowships for Young Scientists to D.T. (1811234) and K.T. (211438). This work was also supported in part by Global Center of Excellence Program from MEXT. We thank M. Takeda for discussions and comments and H. Kasahara, R. Fujimichi, T. Matsui, and K. W. Koyano for advice and help with experiments.

Supporting Online Material

www.sciencemag.org/cgi/content/full/331/6023/1443/DC1
Materials and Methods
SOM Text
Figs. S1 to S9
Tables S1 and S2
References

3 November 2010; accepted 8 February 2011
10.1126/science.1199967

A Brief Social-Belonging Intervention Improves Academic and Health Outcomes of Minority Students

Gregory M. Walton[1]* and Geoffrey L. Cohen[1,2]

A brief intervention aimed at buttressing college freshmen's sense of social belonging in school was tested in a randomized controlled trial ($N = 92$), and its academic and health-related consequences over 3 years are reported. The intervention aimed to lessen psychological perceptions of threat on campus by framing social adversity as common and transient. It used subtle attitude-change strategies to lead participants to self-generate the intervention message. The intervention was expected to be particularly beneficial to African-American students ($N = 49$), a stereotyped and socially marginalized group in academics, and less so to European-American students ($N = 43$). Consistent with these expectations, over the 3-year observation period the intervention raised African Americans' grade-point average (GPA) relative to multiple control groups and halved the minority achievement gap. This performance boost was mediated by the effect of the intervention on subjective construal: It prevented students from seeing adversity on campus as an indictment of their belonging. Additionally, the intervention improved African Americans' self-reported health and well-being and reduced their reported number of doctor visits 3 years postintervention. Senior-year surveys indicated no awareness among participants of the intervention's impact. The results suggest that social belonging is a psychological lever where targeted intervention can have broad consequences that lessen inequalities in achievement and health.

An important question facing society concerns the origins of inequalities between socially marginalized and nonmarginalized groups. Among the most consequential of inequalities is the poorer school and health outcomes experienced by African Americans, Latino Americans, and other non-Asian ethnic minorities relative to European Americans. These differences occur at all levels of socioeconomic status (*1*–*3*).

Although many structural factors contribute to these inequalities, the present research examines a psychological factor: concern about social belonging. Social belonging—a sense of having positive relationships with others—is a fundamental human need (*4*, *5*). Social isolation, loneliness, and low social status harm not only subjective well-being (*6*) but also intellectual achievement (*7*) and immune function and health (*8*–*11*). Even a single instance of exclusion can undermine well-being (*12*, *13*), intelligence quotient (IQ) test performance, and self-control (*14*).

Members of socially stigmatized groups, such as African Americans, may be relatively more uncertain about their social belonging in mainstream institutions like school and work (*7*). Because their ethnic group is often negatively stereotyped and marginalized, they may be unsure of whether they will be fully included in positive social relationships in these settings (*2*). As the sociologist Erving Goffman wrote, "The central feature of the stigmatized individual's situation in life…is a question of…'acceptance'" (*15*). Uncertainty about belonging, especially when chronic, can undermine minorities' performance (*7*, *16*) and health (*3*, *17*, *18*). Social belonging may thus constitute a psychological lever where targeted intervention could yield broad benefits.

[1]Department of Psychology, Stanford University, Stanford, CA 94305, USA. [2]School of Education and Graduate School of Business, Stanford University, Stanford, CA 94305, USA.

*To whom correspondence should be addressed. E-mail: gwalton@stanford.edu

Supporting Online Material

Subjects

All animal procedures complied with the National Institutes of Health Guide for the Care and Use of Laboratory Animals and were approved by the Institutional Review Committee of the University of Tokyo School of Medicine. The subjects were two adult macaque monkeys (*Macaca mulatta* and *Macaca fuscata*, weighing 10-12 kg). A head holder and a recording chamber for electrophysiological recordings were implanted to the skull under standard aseptic, anesthetic and postoperative treatment protocols (anesthetic: sodium pentobarbital, 3 mg/kg/h, i.v., and xylazine, 2 mg/kg, i.m., supplemented as needed; analgesic: acetaminophen, 20 mg/kg/day, p.o.; prophylactic antibiotic: ampicilin, 100 mg/kg/day, i.m.) (*1-2*). Blood pressure, heart rate and oxygen saturation were monitored continuously during the surgery.

Using a 4.7-T magnetic resonance imaging (MRI) scanner and 100 mT/m actively shielded gradient coils (*1*), we obtained high-resolution structural images of the brain for each monkey (in-plane resolutions, 200×200 μm^2 and 300×300 μm^2 for monkeys P and E, respectively; slice thickness, 1mm).

Behavioral task

The procedure of the pair-association (PA) task was as described in detail previously (*3-5*). Briefly, monkeys were trained to perform a pair-association memory task using a set of 6 pairs of visual stimuli (12 monochrome Fourier descriptors) extending approximately 5˚ x 5˚ (Fig. 1A). Monkeys were trained for several months to learn all the pairings of stimuli. In each trial, following the presentation of a fixation point (0.2˚ in size) on the center of a computer screen for 500 ms, a cue stimulus (one of the 12 visual stimuli) was presented for 500 ms. After a delay period of 2000 ms, two stimuli were presented, one of which was the paired-associate of the cue stimulus, and the other was a distractor. The monkey obtained fruit juice as a reward for correctly touching the paired associate within 1500 ms. Throughout the recording sessions after training, the monkeys' performance was > 90% correct. Eye movements were monitored with a PC-based CCD camera system (*3-6*), and if the eye position deviated more than 1.2˚-1.5˚ (monkey P) or 3˚-3.5˚ (monkey E) from the fixation point, the trial was automatically terminated.

Electrophysiological recordings

Extracellular recordings were conducted using linear-array multicontact electrodes (*7-9*) containing 16/24 recording contacts (impedance, 0.3 - 0.5 MΩ at 1 kHz) with an intercontact spacing of 150/100 μm to obtain unit activities (single- and multi-units) and local field potentials (LFPs). Neuronal activity was measured against a local reference that was close to the electrode contacts (a stainless guide tube or the hypodermic metallic shaft surrounding the multicontact electrode) to minimize far-field contributions to LFPs (*9*).

A linear-array multicontact electrode was inserted through a guide tube, lowered through the dura mater into the brain using a hydraulic microdrive manipulator, and positioned at area 36 (A36) (AP, 17 – 22 mm; ML, 13.5 – 15 mm) (Fig. 1B) (*3-6*). After coarsely positioning the electrode at the target area, we calculated current source-density (CSD) profiles (*7-13*) from the stimulus-evoked LFPs of the initial 50-100 trials of the task (for calculation of CSD profiles, see 'Estimation of cortical layers using CSDs' in Data Analysis section of the SOM), and obtained a finer estimation for the depth of the electrode. Then, the electrode position was adjusted so that neuronal signals were recorded from all cortical layers. Further adjustment of the electrode position was performed before obtaining the data so that at least one single-unit was isolated with as high a signal-to-noise (S/N) ratio as possible. Note that all the data in the present study including the CSD profiles were obtained after the final adjustment of the electrode position. The isolated single-unit activity was monitored online using the standard window discrimination technique throughout the recording (*2-6, 14-15*).

Neuronal signals recorded at each contact of the electrode were first fed into unity-gain operational amplifiers, and then fed into a second-stage amplifier. Each signal was then separated into two channels with different band-pass analog filters, with one channel designed to record higher-frequency spiking activities (250 Hz - 8 kHz), ('spike-channel'), and the other designed to record lower frequency field potentials (0.7 - 170 Hz), ('field-channel') (*16*). For both the spike- and field-channels, a 1-pole Butterworth high-pass filter and a 4-pole Butterworth low-pass filter were used. These signals were digitized through a digital acquisition card, and were stored in a PC with a sampling rate of 31-40 kHz for later off-line analysis. At the end of each recording session, the anteroposterior and lateromedial coordinates of the electrode track were measured by x-ray imaging (*2-6*). In six penetrations (three penetrations in monkey E

and three penetrations in monkey P), multiple electrolytic lesions were made (*1-2*) by passing a direct current (10-20 μA for 10-30 s) at pre-selected contacts in each penetration. The lesion marks were identified by histological examinations following all the recordings for each monkey (Table S1).

Histological analyses

Histological analysis in the present study followed our standard protocols (*1-2, 5*). In brief, at the end of all the electrophysiological recordings, monkeys were deeply anesthetized with sodium pentobarbital (50-60 mg/kg, intravenous injection) and perfused with 4% paraformaldehyde in phosphate buffer (pH 7.4). The brains were cut into 40-μm-thick coronal sections, parallel to the plane of electrode penetrations. Serial sections were stained with cresyl violet for Nissl staining. For some sections, we additionally conducted Gallyas staining (*17*). The cytoarchitectonic border between A36 and area TE or area 35 was determined according to the criteria described in previous studies (*18-19*). Histological sections were photographed using standard bright-field optics in BZ-9000 microscope.

For penetrations with electrolytic lesion marks, we estimated the center of the lesion mark by fitting an eclipse on it, and utilized the multiple lesion marks on the histological section as references to estimate the laminar position of the electrode contact at which the earliest current sink was observed (see 'Estimation of cortical layers using CSDs' in the 'Data analysis' section) (*13, 20-22*). On the histological sections, we measured the distance between the estimated position of the earliest-sink contact and the center of the granular layer ($D_{\mathrm{ESC\text{-}GLC}}$, Table S1). The thickness of the granular layer (W_{GL}, Table S1) was measured in histological sections containing lesion marks, and then the proportion of $|D_{\mathrm{ESC\text{-}GLC}}|$ to W_{GL} was calculated. In estimating $D_{\mathrm{ESC\text{-}GLC}}$ and W_{GL}, tissue shrinkage was corrected (*1-2, 5*) using the distance between within-penetration lesion marks.

Estimation of penetration angle to the cortex

In electrophysiological recordings, we targeted the portions of A36 where the electrode can be inserted vertically into the cortex with the aid of MR images (*1, 8-9, 13*). For penetrations with lesion marks, the penetration angle to the cortex was more precisely estimated on histological sections by directly measuring the angle between the vertical axis of the cortex and the electrode path which was reconstructed from

within-penetration lesion marks (Table S1). The angles of the remaining penetrations without lesion marks were estimated by overlying the electrode paths into the corresponding histological sections on the basis of the x-ray images of the electrode tracks (*2, 4-5*). Penetrations where the estimated angle between the electrode path and the direction perpendicular to the cortex exceeded 20˚ were not included in the present study (*23-25*).

Database for the cross-correlation analysis

We recorded both single-units (SUs) and multi-units (MUs), and constructed the database of unit-pairs for the cross-correlation analysis as follows.

To obtain SUs in the off-line analysis, the continuous neuronal signals recorded at 'spike-channels' were high-pass (cut-off frequency: 250-420 Hz) filtered digitally and were thresholded for spike detection. Cluster analysis was then conducted using principal components of waveform features (*26-29*), and a cluster with the largest spike amplitude was isolated using Offline Sorter software (*28-29*). Only a unit with a refractory period (> 2 ms) in the auto-correlogram was accepted as an SU (*14, 26*). In addition, a cross-correlogram (CCG) of SU pairs recorded from two contacts with distances of < 0.3 mm ('near contacts') was examined for an artifactual peak at the center bin and symmetrical gaps in the surrounding bins (*26-27*). The peak and gaps (common refractoriness), if present, indicated that the SU pair originated from an identical neuron and therefore, one of the SU with a lower S/N ratio was not included.

To obtain MUs, the continuous neuronal signals recorded at 'spike channels' were band-pass filtered (420 Hz to 8 kHz) digitally, and MU spikes were detected by thresholding the continuous signals (*30-33*) at 4 SDs above the baseline level (*33*). MU activities recorded at 'near contacts' likely contained spikes that originated from an identical neuron (*31, 34*), and thus a unit-pair recorded at 'near contacts' was excluded from the present analysis. Similarly, when each of two MUs recorded at 'near contacts' exhibited a significant CCG peak with a unit (SU or MU) in another contact, a unit-pair with higher CCG peak was included in the database. Note that, when each of two SUs recorded at 'near contacts' showed a significant CCG peak with a unit (SU or MU) recorded at another contact, we included both of the unit-pairs in the database.

A given recorded unit was defined as cue-responsive if the firing rate during the cue-period (80-580 ms from cue onset) was significantly larger than that during the fix-period at least for one of the cue stimuli (paired *t* test, $P < 0.05$) (*14-15*), and was defined as delay-responsive if the firing rate during the delay-period (500-2000 ms from

cue offset) was significantly larger than that during the fix-period at least for one of the cue stimuli (paired *t* test, $P < 0.05$). The unit exhibiting a significant response either in the cue- or delay-period was referred to as a responsive unit. Unit-pairs were included in the database for the cross-correlation analysis if both of the constituent units exhibited significant responses to at least one common stimulus during a common task-period (cue- and/or delay-periods) and if the available spikes for each constituent unit exceeded 500 (*14-15*).

Data Analysis

Data were analyzed offline using Matlab. Only the data obtained for correct trials were included in further analyses. All of the statistical tests in the present study were two-sided unless otherwise stated.

Estimation of cortical layers using CSD

CSD, either at each trial or averaged across trials, was calculated from the depth profiles of the stimulus-evoked LFPs using a three-point-formula that approximates the second spatial derivative of the voltage recorded at each recording contact (*11-12*). CSD analysis provides a physiological index of the location, direction and density of transmembrane current flow of the corresponding depths of the cortex (*10-12*). CSD at the n-th contact, D_n, was calculated as follows:

$$D_n = -[\varphi(n+1) + \varphi(n-1) - 2\varphi(n)] / \Delta^2,$$

where $\varphi(n)$ is the LFP signal at the n-th contact of the electrode, and Δ is the spacing between the neighboring electrode contacts (150 or 100 μm for the electrode with 16 or 24 contacts, respectively). Negative or positive D_n indicates the current sink or current source at the n-th contact, respectively. In fig. S1, we presented CSDs calculated by the second-nearest technique (*11*) for display purpose.

To physiologically estimate the position of the granular layer, we determined the earliest current sink as follows. First, in each trial, an instantaneous amplitude of CSD at each contact was calculated using a 10 ms time window that was slid in 1 ms steps. Then, we determined the response latency of a CSD for each contact as the first time point after cue onset when the instantaneous amplitude of the CSD was significantly larger than the corresponding value measured at the cue onset (paired *t* test, $P < 0.001$) for at least three consecutive bins. We thus determined the earliest significant current

sink, and utilized the earliest-sink contact as a physiological marker of the granular layer (for histological verification, see Table S1). The contacts superficial to the earliest-sink contact were estimated to be located in the supragranular layer (SG), and the contacts in deeper positions than the earliest-sink contact were estimated to be located in the infragranular layer (IG). Note that we did not include unit data recorded at the neighboring (< 0.3 mm) contacts on both sides of the earliest-sink contact in further analyses (*35-36*) except for the case where we calculated the functional connectivity between units without categorizing the recorded units into G, SG and IG units (Fig.4). Although we did not estimate the border between the cortex and the white matter, a recorded unit was regarded as being located in the cortex if the unit exhibited a significant response during either the cue- or delay-period. In fig. S1, we presented CSD profiles of all the penetrations for which we carried out the cross-correlation analysis.

Cross-correlation analysis

We conducted cross-correlation analysis between spike trains (*14-15, 37-39*) for a given unit-pair using stimuli to which both the constituent units elicited significant responses during either the cue- or delay-period. We constructed raw cross-correlograms (CCGs) for lag times within 100 ms (1 ms resolution) using spikes recorded during a 500 ms period immediately before cue onset (fix-period), during a 500 ms period beginning 80 ms after cue onset (cue-period) and during a 1500 ms period beginning 500 ms after cue offset (delay-period).

In evaluating the strength of spike correlation, trial-to-trial variability in the firing rate and/or response latency is a potential source of estimation bias (*40-41*). To correct for these effects, we calculated an instantaneous firing rate (IFR) predictor of spike correlation (*41*) as follows. First, we convolved raw spike trains with a gaussian kernel (σ = 10 ms) in each trial, and calculated a CCG between these convolved spike trains to obtain the IFR predictor, which estimated the strength of spike correlation due to co-modulation of firing rates within a given trial. This IFR predictor was then subtracted from the raw CCG for each trial, and this calculation was repeated for all trials to compile the IFR-predictor-subtracted CCG, in which the above effects of response variabilities were corrected. The peak of the IFR-predictor-subtracted CCG was detected within ±10 ms lags (*14-15, 35, 42*), and the peak height was evaluated by calculating z-score using the number of spikes for each unit, bin width, and the total recording time (*39, 42-45*). The CCG peak was determined to be statistically significant if the z-score of the peak exceeded a value corresponding to $P = 0.05$ (one-tailed, $Z > 2.82$, corrected for multiple comparisons within ±10 ms lags) (*14-15*).

To measure the net signal flow across cortical layers in each task period, we constructed population-averaged CCGs by averaging the z-scored CCGs of individual pairs with a significant peak (Fig. 2, A and E, fig. S3) (*46-47*). For the population-averaged CCG during the fix-period, individual CCGs were included if the CCG peak of a given unit pair was significant during either the cue- or delay-period. To evaluate the statistical significance of the population-averaged CCG, we tested whether the areas of individual CCGs (*48-50*) within ±10 ms lags (*50*) were larger than 0 (paired *t* test). We also compiled the population-averaged CCGs using correlation coefficient of individual CCGs (*39, 51-54*) instead of z-score (fig. S4). In this calculation, we have added a criterion for the least number of trials as in previous studies using correlation coefficient (*51, 53*) to correct for large variance due to the shortage of the number of trials. We have calculated correlation coefficient for unit pairs if the spikes were collected for at least 100 trials (*51, 53*).

Calculation of Correlation Strength, Asymmetry Index and Center of Mass

To quantify the strength of functional connectivity between recorded units, correlation strength (CS) (*27, 47, 55-56*) was defined for each z-scored CCG as follows.

$$CS = R + L,$$

where R and L indicate the summed z-scores for the bins on the right and left sides of the CCG within 10 ms lags, respectively. The z-score of the center bin (0 ms lag) were equally divided into R and L, and the bins with a negative z-score were not included in the calculation.

To infer the direction of functional connectivity between recorded units, we calculated asymmetry index (AI), which quantified the asymmetry of the CCG peak area against the zero time lag (*15, 57-58*). AI value for each CCG was calculated as follows.

$$AI = (R - L)/(R + L)$$

We also calculated the center of mass (CoM) of the CCGs (*59-61*) to evaluate the directional bias of neuronal interactions. CoMs were calculated according to (*59*), since we subtracted the stimulus-locked component (IFR-predictor) from a raw CCG as in (*59*).

Temporal dynamics of neuronal correlation between SG-unit and IG-unit

We examined the temporal dynamics of functional connectivity between individual SG-IG unit-pairs with a significant CCG peak either in the cue- or delay-period using a sliding time window ('time-resolved CCG') (Fig. 3) (*14, 45, 62*). The time-resolved

CCG at 0 ms was calculated using spikes during the 500 ms window, which started from 250 ms before cue onset. This 500 ms window was then successively shifted in steps of 50 ms (Fig. 3, A and B). The time-resolved CCGs that did not meet the criteria for the number of spikes (> 100 spikes for each unit in each time window) were not included in calculating the population average dynamics in Fig. 3B.

Analysis of single-unit responses in SG and IG

To quantify the dynamics of neuronal activities in SG and IG, we calculated the firing rates of cue-responsive single-units and delay-responsive single-units (fig. S6). In estimating the firing rate, the delay-period was subdivided into three consecutive epochs of 500 ms duration (delay 1, delay 2 and delay 3). The firing rate in each epoch was normalized to the corresponding value during the fix-period (*63-64*) as follows:

Normalized firing rates (task epoch) = Response (task epoch) / Response (fix),

where 'Response' represents the average firing rate in each epoch.

AI- and CS-matrices

Laminar connectivity matrices (*35, 65-66*) were calculated in terms of the strength (CS) and direction (AI) of the functional connectivity between recorded units (CS- and AI-matrices; Fig. 4, A and B). For each unit-pair, the constituent units were categorized into the putative source- and target-units according to the sign of AI. Then, the AI and CS values for each unit-pair were allocated to the corresponding voxels (voxel size; 0.15 mm) of the matrices to obtain the average value across unit-pairs for each voxel. Unit-pairs recorded by the electrode with 24 contacts (intercontact spacing, 100 μm) were interpolated into the corresponding voxels.

Supplementary results

Cross-correlation results and pair-types

In Fig. 2, data from SU-SU, SU-MU and MU-MU pairs were merged to examine the direction of the net signal flow across cortical layers. We here present the results of cross-correlation analysis for MU-MU pairs and SU-SU/SU-MU pairs (SU-SU and SU-MU pairs were merged due to a small number of SU-SU pairs).

For SG-IG pairs, AIs were compared between SU-SU/SU-MU pairs and MU-MU pairs, and no significant differences were observed [Wilcoxon signed-rank test; cue-period, $P > 0.2$, median = 0.18 (n = 24) and 0.22 (n = 17) for SU-SU/SU-MU pairs and MU-MU pairs, respectively; delay-period, $P > 0.9$, median = -0.14 (n = 18) and

-0.13 (n = 23)]. Similarly, CoMs were compared between SU-SU/SU-MU pairs and MU-MU pairs, and no significant differences were observed [Wilcoxon signed-rank test; cue-period, $P > 0.4$, median = 1.6 ms (n = 24) and 1.6 ms (n = 17) for SU-SU/SU-MU pairs and MU-MU pairs, respectively; delay-period, $P > 0.3$, median = -0.3 ms (n = 18) and -1.8 ms (n = 23)]. To test whether the reversal of signal flow between SG and IG could occur with only SU-SU pairs, we added a substantial number of SU-SU pairs (see the legend of fig. S5 for the procedures), and found that these SU-SU pairs by themselves revealed significant directional biases in the spike correlation depending on the task periods: SG to IG during the cue-period, IG to SG during the delay-period (fig. S5).

For G-SG pairs, AIs showed no significant differences between SU-SU/SU-MU pairs and MU-MU pairs in either the cue- or delay-period [Wilcoxon signed-rank test; cue-period, $P > 0.4$, median = 0.17 (n = 10) and 0.22 (n = 7) for SU-SU/SU-MU and MU-MU pairs, respectively; delay-period, $P > 0.6$, median = 0.02 (n = 5) and 0.10 (n = 9)]. Similarly, CoMs of G-SG pairs showed no significant differences between SU-SU/SU-MU pairs and MU-MU pairs in either the cue- or delay-periods [cue-period, $P > 0.1$, median = 3.4 ms (n = 10) and 1.2 ms (n = 7) for SU-SU/SU-MU and MU-MU pairs, respectively; delay-period, $P > 0.3$, median = 1.3 ms (n = 5) and 0.1 ms (n = 9)]. AIs of G-IG pairs showed no significant differences between SU-SU/SU-MU pairs and MU-MU pairs in either the cue- or delay-periods [cue-period, $P > 0.9$, median = 0.15 (n = 8) and -0.01 (n = 6); delay-period, $P > 0.6$, median = -0.01 (n = 8) and -0.07 (n = 7)]. Similarly, CoMs of G-IG pairs showed no significant differences between SU-SU/SU-MU pairs and MU-MU pairs in either the cue- or delay-periods [cue-period, $P > 0.8$, median = 1.3 ms (n = 8) and 2.1 ms (n = 6); delay-period, $P > 0.5$, median = 0.4 ms (n = 8) and -1.0 ms (n = 7)].

Next, we calculated the proportions of SG-IG pairs that changed the signs of AI between the cue- and delay-periods (‘flipped pairs’ in Fig. 3, C and D) separately for SU-SU/SU-MU and MU-MU pairs. No significant differences were observed in the proportions of flipped pairs between SU-SU/SU-MU and MU-MU pairs [χ^2 test, $P > 0.9$, 43% (17/40 pairs) and 53% (16/30 pairs) for SU-SU/SU-MU and MU-MU pairs, respectively]. We also compared the proportions of flipped pairs that showed positive AIs (SG to IG) in the cue-period and negative AIs (IG to SG) in the delay-period between SU-SU/SU-MU and MU-MU pairs. No significant difference was observed in the proportions of pairs with positive AIs between these two groups of unit-pairs [χ^2 test, $P > 0.9$, 71% (12/17 pairs) and 75% (12/16 pairs) for SU-SU/SU-MU pairs and MU-MU pairs, respectively].

Cross-correlation results for each monkey

Correlation analyses shown in Fig. 2 were repeated by separating our database into those from individual monkeys.

AIs of SG-IG pairs with a significant CCG peak showed no significant difference between monkeys in either the cue- or delay-period [Wilcoxon signed-rank test; cue-period, $P > 0.1$, median = 0.39 (n = 15) and 0.18 (n = 26) for monkeys E and P, respectively; delay-period, $P > 0.2$, median = -0.10 (n = 16) and -0.16 (n = 25)]. CoMs of SG-IG pairs with a significant CCG peak showed no significant difference between monkeys in either the cue- or delay-periods (cue-period, $P > 0.1$, median = 2.5 ms and 1.3 ms for monkeys E and P, respectively; delay-period, $P > 0.8$, median = -1.5 ms and -1.6 ms).

During the cue-period, AIs of SG-IG pairs revealed the same tendency of directional bias (SG to IG) for each monkey (monkey E, $P < 0.01$; monkey P, $P = 0.08$). CoMs also revealed the same tendency (monkey E, $P < 0.02$; monkey P, $P = 0.37$). During the delay-period, AIs of SG-IG pairs revealed the same tendency of directional bias (IG to SG) for each monkey (monkey E, $P < 0.05$; monkey P, $P = 0.08$). CoMs also revealed the same tendency (monkey E, $P = 0.10$; monkey P, $P = 0.08$).

AIs of G-SG pairs were not significantly different between monkeys in any of the task periods [cue-period, $P > 0.2$, median = 0.09 (n = 6) and 0.21 (n = 11); delay-period, $P > 0.2$, 0.27 (n = 4) and 0.06 (n = 10)]. CoMs of G-SG pairs were not significantly different between monkeys in any of the task periods (cue-period, $P > 0.3$, median = 0.3 ms and 3.4 ms; delay-period, $P > 0.3$, -0.4 ms and 1.0 ms). AIs of G-SG pairs in the cue-period revealed the same tendency of directional bias (G to SG) for each monkey (monkey E, $P = 0.39$; monkey P, $P < 0.05$). CoMs revealed the same tendency (monkey E, $P = 0.34$; monkey P, $P < 0.05$).

AIs of G-IG pairs were not significantly different between monkeys [cue-period, $P > 0.5$, median = 0.16 (n = 7) and 0.14 (n = 7); delay-period, $P > 0.2$, -0.16 (n = 6) and 0.02 (n = 9)]. CoMs of G-IG pairs were not significantly different between monkeys (cue-period, $P > 0.4$, median = 3.4 ms and 0.8 ms; delay-period, $P > 0.5$, 0.4 ms and -1 ms).

Next, we calculated the proportions of SG-IG pairs that changed their signs of AI between the cue- and delay-periods ('flipped pairs' in Fig. 3C) separately for individual monkeys. The proportions of flipped pairs were not significantly different between monkeys [χ^2 test, $P > 0.6$, 44% (12/27 pairs) and 49% (21/43 pairs) for monkeys E and P, respectively]. We also compared the proportions of flipped pairs that showed positive

AIs (SG to IG) in the cue-period and negative AIs (IG to SG) in the delay-period between the monkeys, and did not find a significant difference [χ^2 test, $P > 0.7$, 75% (9/12 pairs) and 71% (15/21 pairs)].

Estimation of negative neuronal correlation

For G-SG pairs in Fig. 2, only two pairs and one pair of units revealed significant negative cross-correlations (the criterion for detecting a significant negative neuronal correlation was the same as that for the positive neuronal correlation, but the opposite in sign) during the cue- and delay-periods, respectively. Similarly, for SG-IG pairs, only one pair and three pairs of units revealed significant negative cross-correlations during the cue-and delay-periods, respectively.

Single-unit responses in SG and IG

We examined whether the firing rates of the SG-unit reflected the signal flow from IG during the delay-period. The firing rates of IG single-units (n = 27) selectively responded throughout the delay-period (fig. S6C) (paired *t* test with Bonferroni's correction, $P < 0.01$). By contrast, the responses of SG single-units (n = 13) developed during the latter part of the delay-period (fig. S6D) (two-way ANOVA followed by Tukey's test; time × stimulus interaction, $P < 0.05$), consistent with the gradual appearance of signal flow from IG to SG (Fig. 3, A and B) (for the relation between the connectivity direction of unit-pairs and the firing rates of the constituent units, see fig. S7).

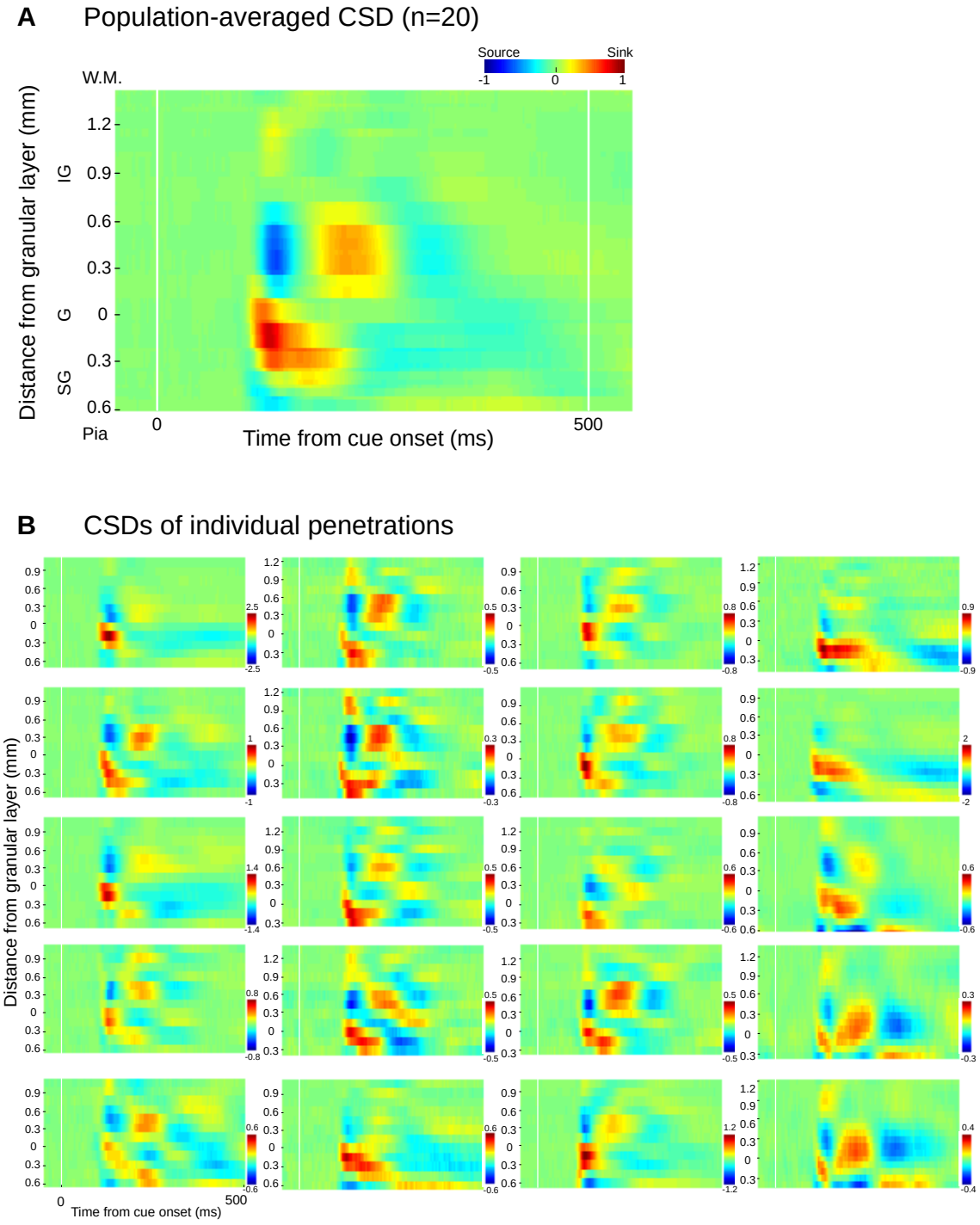

Fig. S1. CSD profiles of all penetrations. (**A**) Population-averaged CSDs (n = 20). All penetrations were aligned along the cortical depth at the earliest-sink contact. Individual CSDs were normalized by the maximum value of CSDs within each penetration. (**B**) CSD profiles of individual penetration. CSD amplitude at cue onset (baseline level) was subtracted from the time course of CSD amplitude in each contact.

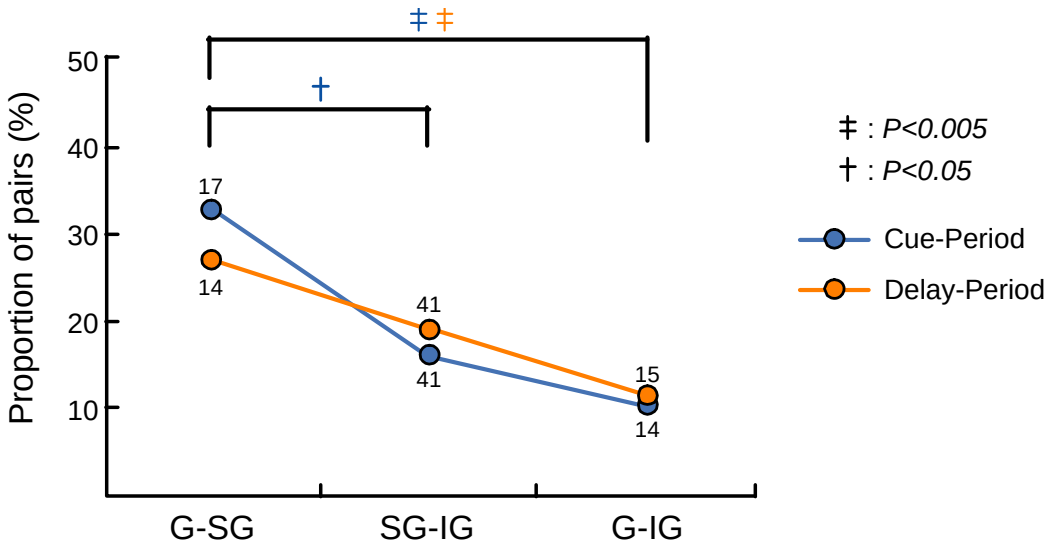

Fig. S2. Proportion of unit-pairs with significant CCG peak in the G-SG, SG-IG and G-IG pairs. The number on each circle indicates the number of unit-pairs that showed significant CCG peak. Proportion of unit-pairs with significant CCG peak ($Z > 2.82$, $P < 0.05$; one-tailed, corrected for multiple comparisons within ±10 ms lags) was compared among G-SG, SG-IG and G-IG both in the cue- (blue) and delay- (orange) periods using χ^2 test followed by post hoc pair-wise comparisons with corrections for multiple comparisons by the Bonferroni's method. Colors of daggers indicate task-periods.

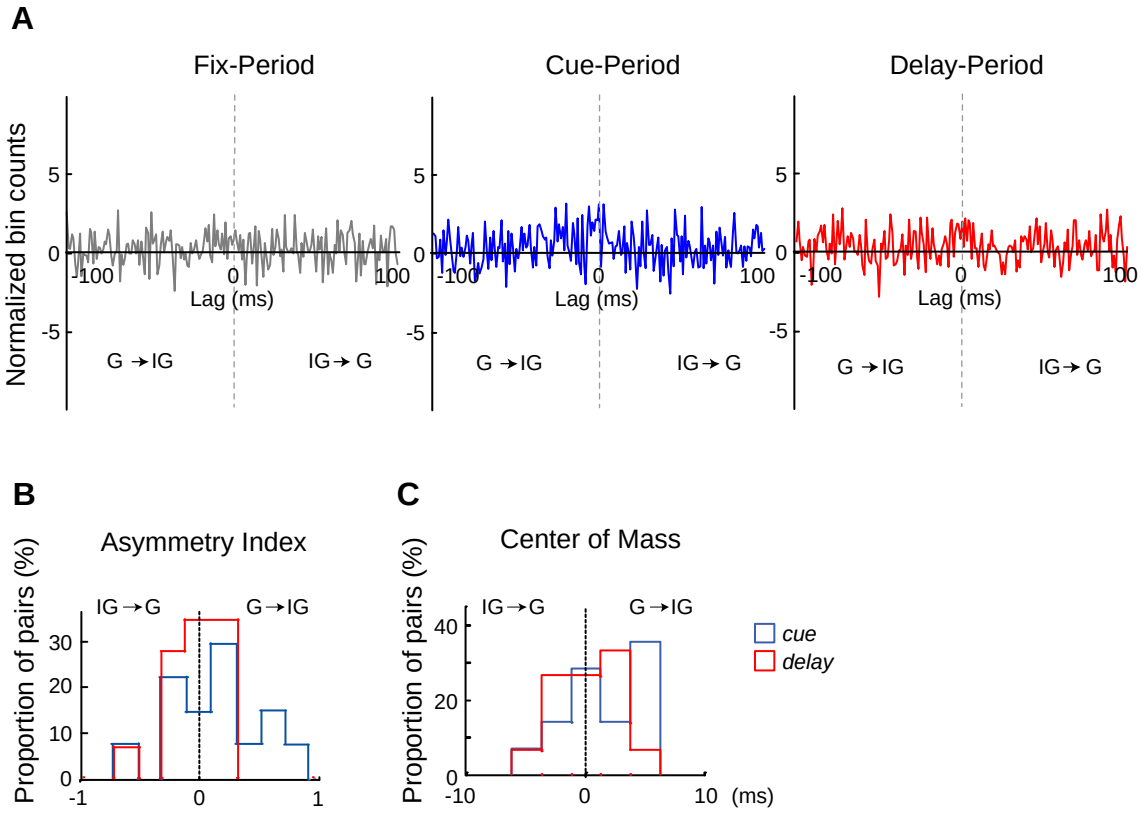

Fig. S3. Population results of the functional connectivity for G-IG pairs. Calculation procedure and display format is the same as in Fig. 2. (**A**) Population-averaged CCGs showed no significant peak in either of the task period. (**B** and **C**) Distributions of AIs (B) and CoMs (C) showed no bias in either of the task period.

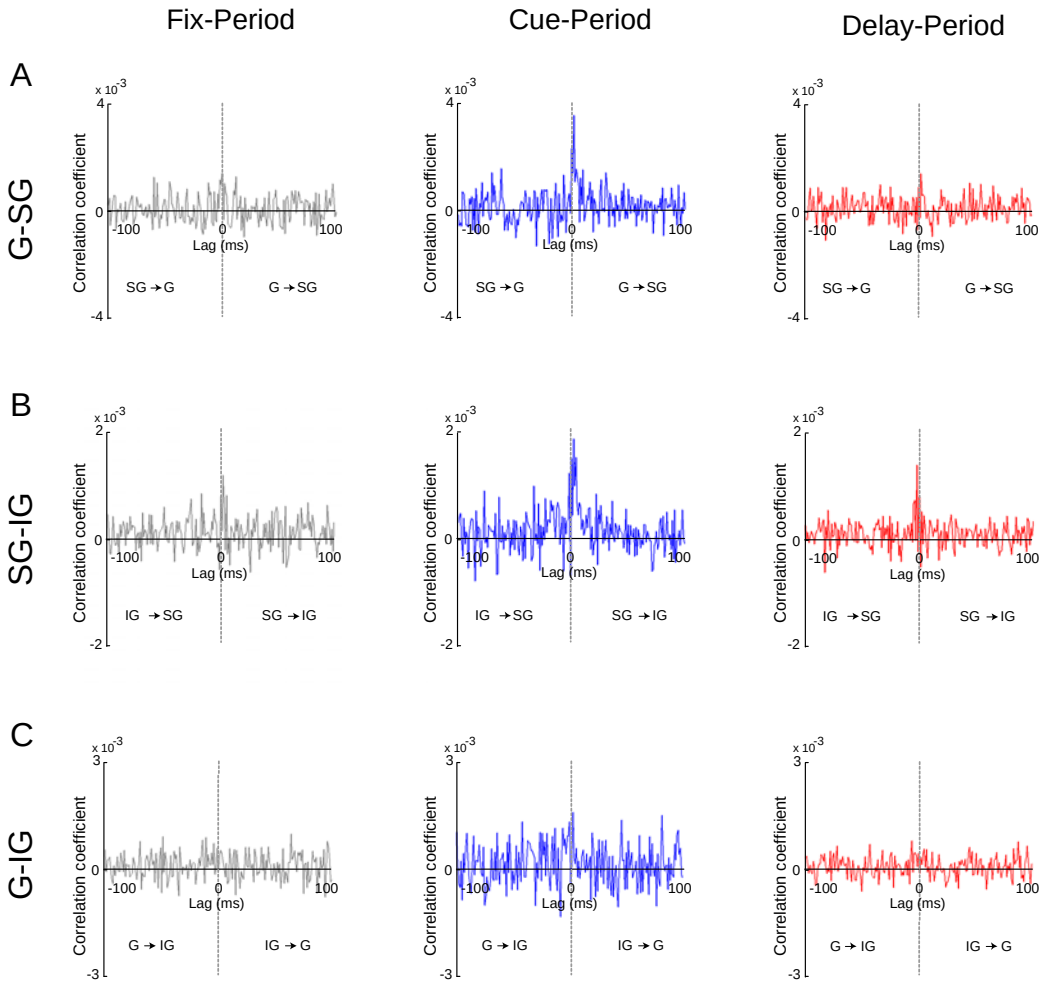

Fig. S4. Population-averaged CCGs using correlation coefficient for G-SG (**A**), SG-IG (**B**) and G-IG (**C**) pairs in each task period.

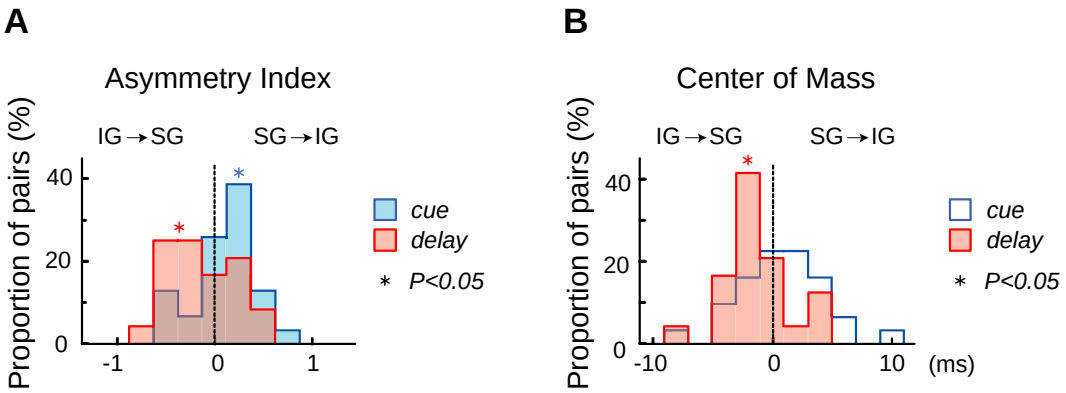

Fig. S5. Functional connectivity between SG and IG using only single-units. In addition to the original SG-IG database (Fig. 2, E to G), we constructed a new SG-IG database consisting exclusively of single-unit pairs, and calculated asymmetry index (**A**) and center of mass (**B**) of unit-pairs with significant CCG peak during the cue- and delay-periods (cue-period, 31 pairs; delay-period, 24 pairs). To construct the new single unit database, we re-sorted single-units by applying a new criterion (maximum proportion of spikes with the ISI < 2 ms increased from 0.7% to 1.0%), and applied a lower threshold for detecting the CCG peak, that is, $P < 0.05$ without correction for multiple comparisons among different bins. CCGs were calculated only when the available spikes exceeded 700 for each unit to obtain a reliability of the resultant CCGs. Asterisk, significant bias to either side of the histogram. Filled histogram, the task period for which significant bias in the directionality was observed. The same biases of functional connectivity as those in the original SG-IG database were observed in each task period [AI: cue-period, median = 0.16, $P < 0.05$, Wilcoxon signed-rank test; delay-period, median = -0.22, $P < 0.05$; CoM: cue-period, median = 0.8 ms, $P = 0.15$; delay-period, median = -1.8 ms, $P < 0.05$]. During the fix-period, no directional bias was observed (AI: median = -0.03, $P > 0.3$, n= 13; CoM: median = -0.8 ms, $P > 0.5$).

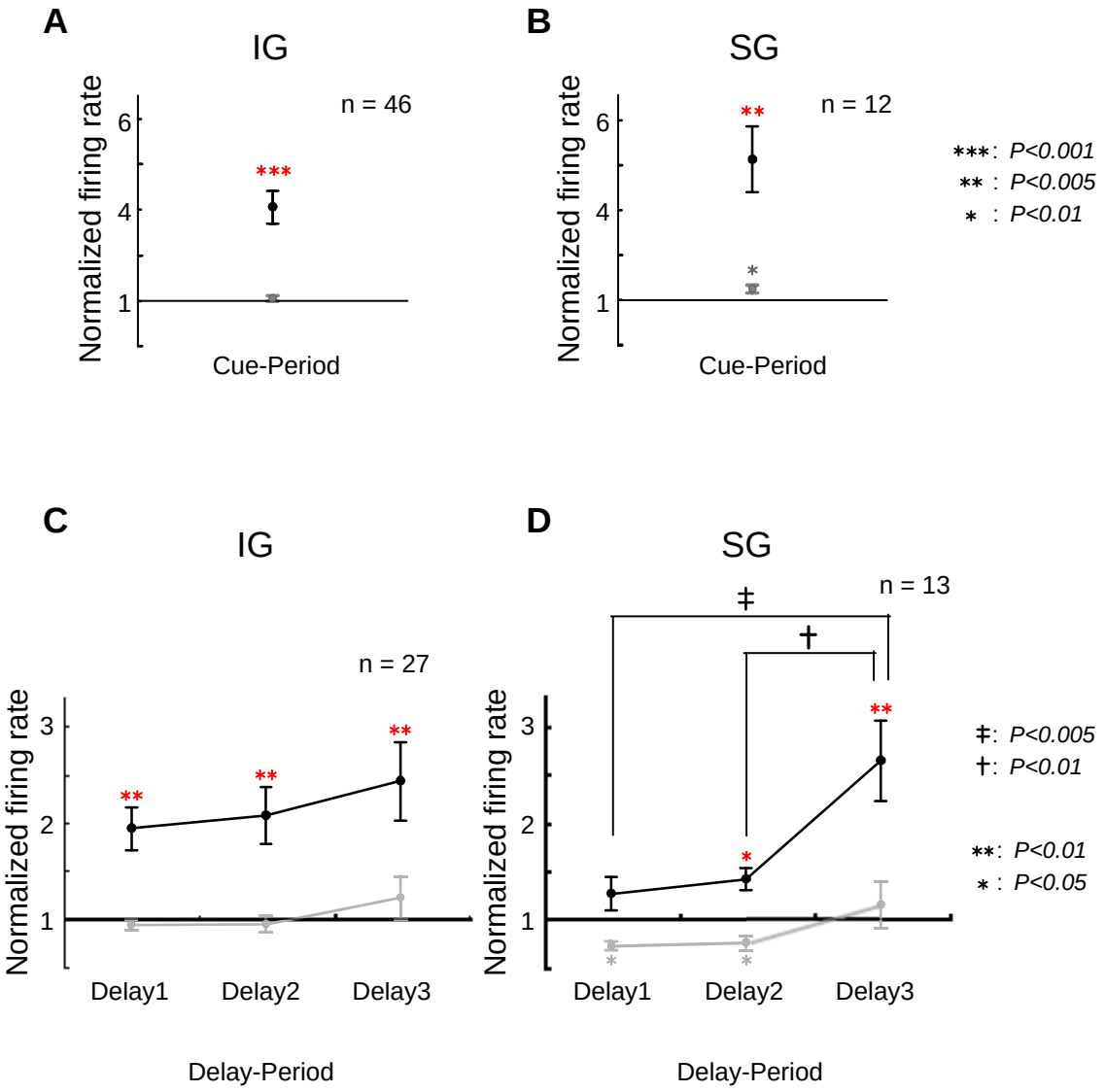

Fig. S6. Neuronal responses in IG and SG. (**A** and **B**) Firing rates of the cue-responsive single-units in IG (**A**) and SG (**B**) during the cue-period. (**C** and **D**) Firing rates of the delay-responsive single-units in IG (**C**) and SG (**D**) during the delay-period. For each unit, firing rates were calculated using the best (black) and worst (gray) stimuli (the stimuli that elicited the largest and smallest responses during the cue/delay-period, respectively), and were normalized by the firing rate in the fix-period. In (B), a neuron was excluded from the dataset as an outlier (Smirnov-Grubbs test, $P < 0.01$, n = 13). Firing rate of a delay-responsive single-unit (C and D) was calculated for three consecutive 500 ms time windows (delay 1, delay 2 and delay 3) during the delay-period (from 500 ms to 2000 ms following cue offset). For delay-responsive IG

units (C, n = 27), significant responses were observed throughout the delay-period (delay 1-3) (paired *t* test, corrected for multiple comparisons across different time windows, $P < 0.001$). For delay-responsive SG units (D, n = 13), the two-way ANOVA on stimulus condition (best stimulus vs. worst stimulus) and time (delay 1-3) revealed a significant interaction between stimulus and time window [$F(2,60) = 3.27$, $P < 0.05$]. Post-hoc pair-wise comparisons revealed that SG-units showed significantly larger responses in delay 3 than in delay 1 and 2 (Tukey's test). Error bars represent SEM. Daggers indicate statistical significance assessed by post-hoc Tukey's test. Asterisks indicate statistical significance assessed by paired *t* test, corrected for multiple comparisons across different time windows.

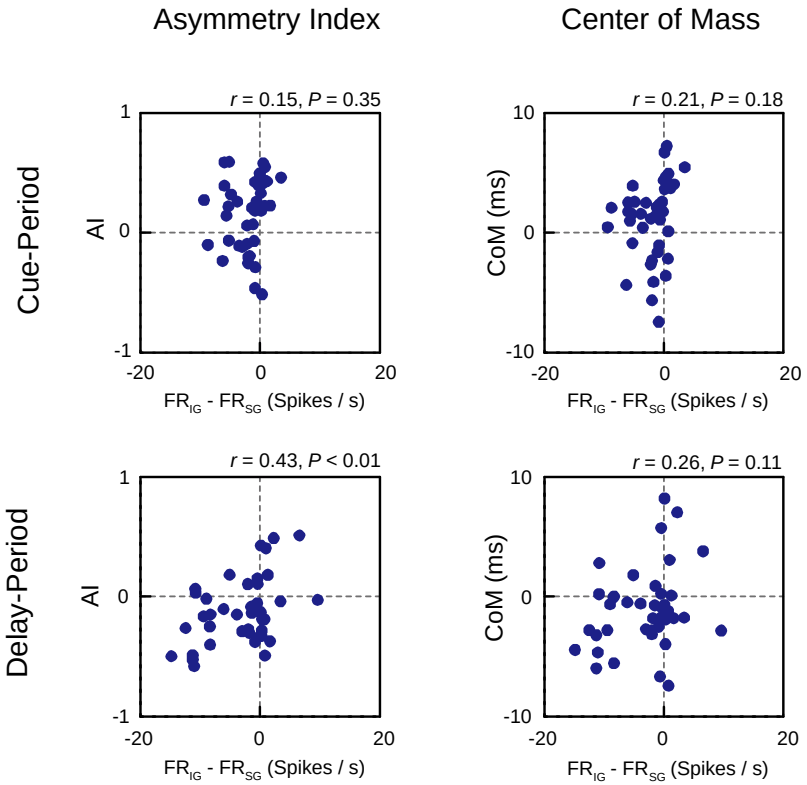

Fig. S7. Relation between the direction of functional connectivity of SG-IG pairs and the firing rates of constituent units. AIs (left column) and CoMs (right column) were plotted against the difference of the firing rates (FR) between IG and SG units in each task period.

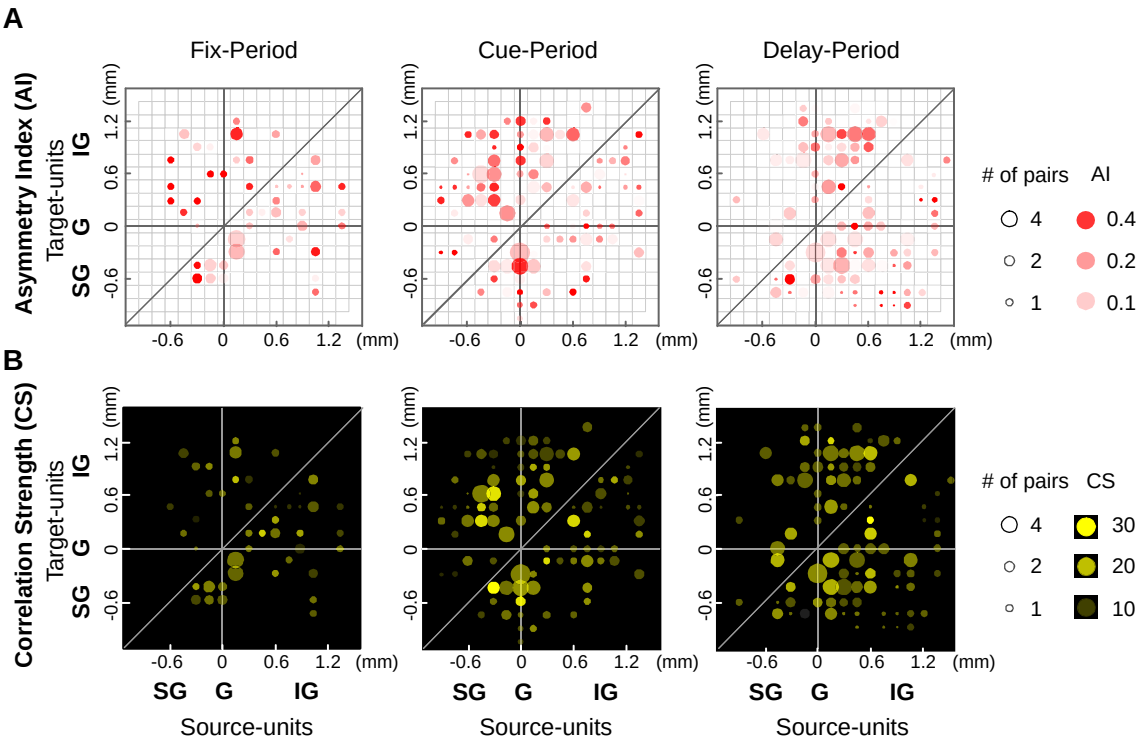

Fig. S8. Interlaminar connectivity matrices [AI- (**A**) and CS-matrices (**B**)] during each task period. Calculation procedure and display format are the same as in Fig. 4 except that the size of a circle in each matrix indicates the number of unit-pairs with significant CCG peak. Blank voxels (three voxels in upper-left and three voxels in lower-right) in each matrix correspond to laminar positions that were not recorded in the present study.

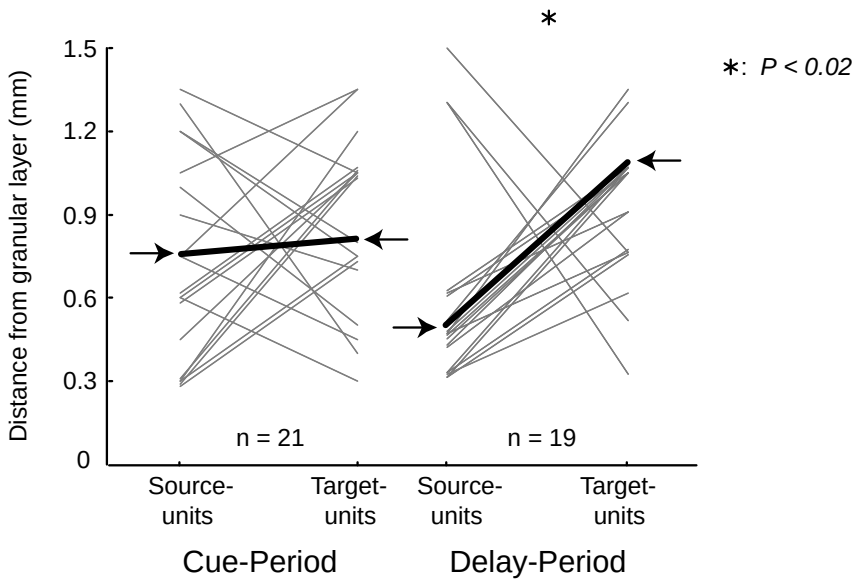

Fig. S9. Functional connectivity within IG during the cue- and delay-periods. Both of the constituent units of a pair were recorded in IG. The putative source- and target-units that showed significant CCG peak during the cue-period showed no difference in their recorded positions. In contrast, during the delay-period, putative target-units were located at positions significantly deeper than the putative source-units (paired *t* test, $P < 0.02$, n = 19 pairs). Arrows represent median values. Overlapped lines were shifted for presentation purpose. Unit-pairs with AI values within the range of -0.2 and 0.2 were excluded in this analysis (56). Results did not change when we repeated the same analysis using all unit-pairs (cue-period, $P > 0.5$, n = 37 pairs; delay-period, $P < 0.05$, n = 39 pairs).

Table S1. Summary for the histological analysis.

Track	Subject	$A_{E\text{-}CTX}$ (deg)	$D_{ESC\text{-}GLC}$ (μm)	$\lvert D_{ESC\text{-}GLC}\rvert$ (μm)	W_{GL} (μm)	$\lvert D_{ESC\text{-}GLC}\rvert/W_{GL}$ (%)
#1	E	5	+65	65	185	35
#2	E	11	+17	17	200	9
#3	E	15	+13	13	220	6
#4	P (R)	12	-99	99	210	47
#5	P (L)	4	-100	100	220	45
#6	P (L)	3	+92	92	195	47
	Mean	8.3	-2	64	205	32
	Median	8.0	+15	79	205	40
	S.D.	5.0	81	40	14	19

R, right hemisphere; L, left hemisphere; $A_{E\text{-}CTX}$, electrode penetration angle to cortex; $D_{ESC\text{-}GLC}$, signed distance between the earliest-sink contact and granular layer center; +, deviation to supragranular; -, deviation to infragranular; $\lvert D_{ESC\text{-}GLC}\rvert$, absolute value of $D_{ESC\text{-}GLC}$; W_{GL}, width of granular layer; $\lvert D_{ESC\text{-}GLC}\rvert/W_{GL}$, proportion of $\lvert D_{ESC\text{-}GLC}\rvert$ to W_{GL}.

Table S1. Summary for the histological analysis. Penetration angle to the cortex ($A_{E\text{-}CTX}$) was estimated by measuring the angle between the vertical axis of the cortex (alignments of cells in radial direction) and the electrode path which was reconstructed from within-penetration lesion marks. Laminar position of the earliest-sink contact was estimated using lesion marks, and overlain on the histological section. Then, the signed distance between the positions of the earliest-sink contact and the granular layer center ($D_{ESC\text{-}GLC}$) was estimated. The thickness of the granular layer (W_{GL}) was also measured for each penetration, and then proportion of $\lvert D_{ESC\text{-}GLC}\rvert$ to W_{GL} was calculated ($\lvert D_{ESC\text{-}GLC}\rvert/W_{GL}$) (for details, see 'Histological analyses' section in SOM).

Table S2. Database of unit-pairs for cross-correlation analysis.

		Fix-Period	Cue-Period	Delay-Period
G-SG	SU-SU	2	5	5
	SU-MU	13	18	17
	MU-MU	28	29	27
Total (# of pairs)		43	52	49

		Fix-Period	Cue-Period	Delay-Period
G-IG	SU-SU	8	12	12
	SU-MU	40	51	55
	MU-MU	64	65	54
Total (# of pairs)		112	128	121

		Fix-Period	Cue-Period	Delay-Period
SG-IG	SU-SU	15	31	25
	SU-MU	74	102	98
	MU-MU	108	119	88
Total (# of pairs)		197	252	211

Table S2. Database of unit-pairs for cross-correlation analysis. G, granular layer; SG, supragranular layer; IG, infragranular layer; SU, single-unit; MU, multi-unit. Numbers of G-SG, G-IG and SG-IG pairs analyzed in each task period were presented. A CCG was calculated for each unit-pair for each task-period, and was included into the database if the available spikes for each constituent unit during a given period exceeded 500.

Supporting References

S 1. T. Matsui *et al.*, *Nature Methods* **4**, 161 (2007).

S 2. R. Fujimichi *et al.*, *Eur. J. Neurosci.* **32**, 659 (2010).

S 3. Y. Naya, M. Yoshida, Y. Miyashita, *Science* **291**, 661 (2001).

S 4. Y. Naya, M. Yoshida, Y. Miyashita, *J. Neurosci.* **23**, 2861 (2003).

S 5. M. Yoshida, Y. Naya, Y. Miyashita, *Proc. Natl. Acad. Sci. U.S.A.* **100**, 4257 (2003).

S 6. M. Takeda, Y. Naya, R. Fujimichi, D. Takeuchi, Y. Miyashita, *Neuron* **48**, 839 (2005).

S 7. C. E. Schroeder, P. Lakatos, *Trends Neurosci.* **32**, 9 (2009).

S 8. S. S. Cash *et al.*, *Science* **324**, 1084 (2009).

S 9. A. Maier, G. K. Adams, C. Aura, D. A. Leopold, *Front. Syst. Neurosci.* **4** (2010).

S 10. C. Nicholson, J. A. Freeman, *J. Neurophysiol.* **38**, 356 (1975).

S 11. J. A. Freeman, C. Nicholson, *J. Neurophysiol.* **38**, 369 (1975).

S 12. U. Mitzdorf, *Physiol. Rev.* **65**, 37 (1985).

S 13. C. E. Schroeder, A. D. Mehta, S. J. Givre, *Cereb. Cortex* **8**, 575 (1998).

S 14. T. Hirabayashi, Y. Miyashita, *J. Neurosci.* **25**, 10299 (2005).

S 15. T. Hirabayashi, D. Takeuchi, K. Tamura, Y. Miyashita, *J. Neurosci.* **30**, 10407 (2010).

S 16. M. J. Nelson, P. Pouget, E. A. Nilsen, C. D. Patten, J. D. Schall, *J. Neurosci. Methods* **169**, 141 (2008).

S 17. F. Gallyas, *Neurol. Res.* **1**, 203 (1979).

S 18. W. A. Suzuki, D. G. Amaral, *J. Comp. Neurol.* **463**, 67 (2003).

S 19. K. S. Saleem, J. L. Price, T. Hashikawa, *J. Comp. Neurol.* **500**, 973 (2007).

S 20. P. Mullerpreuss, U. Mitzdorf, *Hear. Res.* **16**, 133 (1984).

S 21. T. Jellema, C. H. Brunia, W. J. Wadman, *Neuroscience* **129**, 283 (2004).

S 22. L. Uva, M. de Curtis, *Neuroscience* **122**, 843 (2003).

S 23. A. G. Pettigrew, A. D. Ansselin, J. R. Bramley, *Development* **104**, 575 (1988).

S 24. I. Fujita, K. Tanaka, M. Ito, K. Cheng, *Nature* **360**, 343 (1992).

S 25. A. Kral, J. Tillein, S. Heid, R. Hartmann, R. Klinke, *Cereb. Cortex* **15**, 552 (2005).

S 26. J. Csicsvari, H. Hirase, A. Czurko, G. Buzsaki, *Neuron* **21**, 179 (1998).

S 27. M. S. Fee, P. P. Mitra, D. Kleinfeld, *J. Neurosci. Methods* **69**, 175 (1996).

S 28. J. Y. Cohen *et al.*, *J. Neurosci.* **30**, 3227 (2010).

S 29. P. Fries, J. H. Reynolds, A. E. Rorie, R. Desimone, *Science* **291**, 1560 (2001).

S 30. M. Castelo-Branco, R. Goebel, S. Neuenschwander, W. Singer, *Nature* **405**, 685 (2000).
S 31. H. Super, P. R. Roelfsema, *Prog. Brain. Res.* **147**, 263 (2005).
S 32. J. Liu, W. T. Newsome, *J. Neurosci.* **26**, 7779 (2006).
S 33. I. Nauhaus, L. Busse, M. Carandini, D. L. Ringach, *Nature Neurosci.* **12**, 70 (2009).
S 34. C. M. Gray, P. E. Maldonado, M. Wilson, B. McNaughton, *J. Neurosci. Methods* **63**, 43 (1995).
S 35. C. A. Atencio, C. E. Schreiner, *PLoS One* **5**, e9521 (2010).
S 36. S. Sakata, K. D. Harris, *Neuron* **64**, 404 (2009).
S 37. G. L. Gerstein, D. H. Perkel, *Biophys. J.* **12**, 453 (1972).
S 38. A. M. Aertsen, G. L. Gerstein, M. K. Habib, G. Palm, *J. Neurophysiol.* **61**, 900 (1989).
S 39. J. J. Eggermont, *J. Neurophysiol.* **68**, 1216 (1992).
S 40. C. D. Brody, *Neural Comput.* **11**, 1537 (1999).
S 41. S. N. Baker, R. Spinks, A. Jackson, R. N. Lemon, *J. Neurophysiol.* **85**, 869 (2001).
S 42. M. Tomita, J. J. Eggermont, *J. Neurophysiol.* **93**, 378 (2005).
S 43. S. A. Roy, S. P. Dear, K. D. Alloway, *J. Neurosci.* **21**, 1795 (2001).
S 44. A. Thiele, G. Stoner, *Nature* **421**, 366 (2003).
S 45. S. C. de Oliveira, A. Thiele, K. P. Hoffmann, *J. Neurosci.* **17**, 9248 (1997).
S 46. Z. Zhou, M. R. Bernard, A. B. Bonds, *J. Neurosci.* **28**, 3759 (2008).
S 47. H. Super, C. van der Togt, H. Spekreijse, V. A. Lamme, *J. Neurosci.* **23**, 3407 (2003).
S 48. A. Das, C. D. Gilbert, *Nature* **399**, 655 (1999).
S 49. A. Kohn, M. A. Smith, *J. Neurosci.* **25**, 3661 (2005).
S 50. M. A. Smith, A. Kohn, *J. Neurosci.* **28**, 12591 (2008).
S 51. P. R. Roelfsema, V. A. Lamme, H. Spekreijse, *Nature Neurosci.* **7**, 982 (2004).
S 52. J. M. Samonds, B. R. Potetz, T. S. Lee, *J. Neurosci.* **29**, 15780 (2009).
S 53. J. J. Eggermont, *J. Neurophysiol.* **71**, 246 (1994).
S 54. W. Bair, E. Zohary, W. T. Newsome, *J. Neurosci.* **21**, 1676 (2001).
S 55. C. Constantinidis, M. N. Franowicz, P. S. Goldman-Rakic, *J. Neurosci.* **21**, 3646 (2001).
S 56. M. D. Menz, R. D. Freeman, *Nature Neurosci.* **6**, 59 (2003).
S 57. J. M. Alonso, L. M. Martinez, *Nature Neurosci.* **1**, 395 (1998).
S 58. M. D. Menz, R. D. Freeman, *J. Neurophysiol.* **91**, 1794 (2004).

S 59. C. P. Hung, B. M. Ramsden, A. W. Roe, *Nature Neurosci.* **10**, 1185 (2007).
S 60. J. L. Gerrard, S. N. Burke, B. L. McNaughton, C. A. Barnes, *J. Neurosci.* **28**, 7883 (2008).
S 61. A. Luczak, P. Bartho, K. D. Harris, *Neuron* **62**, 413 (2009).
S 62. L. G. Nowak, M. H. Munk, J. I. Nelson, A. C. James, J. Bullier, *J. Neurophysiol.* **74**, 2379 (1995).
S 63. G. Kreiman, C. Koch, I. Fried, *Nature* **408**, 357 (2000).
S 64. L. J. Toth, J. A. Assad, *Nature* **415**, 165 (2002).
S 65. S. Lefort, C. Tomm, J. C. F. Sarria, C. C. H. Petersen, *Neuron* **61**, 301 (2009).
S 66. N. Weiler, L. Wood, J. I. Yu, S. A. Solla, G. M. G. Shepherd, *Nature Neurosci.* **11**, 360 (2008).

Supporting Online Material

www.sciencemag.org
Materials and Methods
Supporting online text
Figs. S1 to S9
Tables S1 and S2